

Universidade de São Paulo
Instituto de Física

Cosmologia de HI e técnicas observacionais avançadas

Pablo César Benevides de Carvalho Rossas Motta

Orientador: Prof. Dr. Elcio Abdalla

Monografia apresentada ao Instituto de Física como requisito
parcial para a qualificação no Curso de Doutorado em Ciê-
ncias.



São Paulo
2024

University of São Paulo
Physics Institute

HI cosmology and advanced observational tools

Pablo César Benevides de Carvalho Rossas Motta

Supervisor: Prof. Dr. Elcio Abdalla

Report submitted to the Physics Institute of the University
of São Paulo for the Doctor of Science Qualifying Exam.

São Paulo
2024

Abstract

Neutral hydrogen (HI) intensity mapping (IM) is opening new ways to explore large-scale structure (LSS) growth and late-time cosmic acceleration, complementing redshift surveys in optical bands. The Baryon Acoustic Oscillations from Integrated Neutral Gas Observations (BINGO) telescope uses HI IM to constrain cosmological parameters. In this work, we apply Bayesian inference to simulate HI IM signals, incorporating systematic effects like foreground residuals, thermal noise, and beam resolution limits. This approach enables precise constraints on six Λ CDM cosmological parameters, with further improvements seen when combining BINGO and Planck 2018 TT,TE,EE+lowE+lensing data.

In addition to improving constraints on cosmological parameters, BINGO offers an exciting opportunity to detect and localize Fast Radio Bursts (FRBs). The next phase of the project, BINGO/ABDUS, will incorporate smaller outrigger radio telescopes to form an interferometric system. We propose that the outrigger telescopes be based on an Aperture Array of Vivaldi Antennas. Electromagnetic simulations are performed for both the prototype tile and the envisioned Vivaldi Aperture Array Outrigger Station (VAAOS). The analysis includes scan angles, effective areas, the effects of beamforming inaccuracies due to time-delay quantization, polarization characteristics, and the emergence of grating lobes at high angles and frequencies.

Palavras-chave: Dark Energy, Large Scale Structure of the Universe, Cosmological parameters, Instrumentation: Detectors, Telescopes

Resumo

O mapeamento de intensidade de hidrogênio neutro (HI) está abrindo novas possibilidades para investigar o crescimento da estrutura em larga escala (LSS) e a aceleração cósmica em tempos tardios, complementando os levantamentos de desvio para o vermelho em bandas ópticas. O telescópio Baryon Acoustic Oscillations from Integrated Neutral Gas Observations (BINGO) utiliza o mapeamento de intensidade de HI para restringir parâmetros cosmológicos. Neste estudo, aplicamos inferência Bayesiana para simular sinais de mapeamento de intensidade de HI, incorporando efeitos sistemáticos como resíduos de fundo, ruído térmico e limites de resolução de feixe. Essa abordagem possibilita restrições precisas em seis parâmetros cosmológicos do modelo CDM, com melhorias adicionais observadas ao combinar os dados do BINGO com os do Planck 2018 TT,TE,EE+lowE+lensing.

Além de aprimorar as restrições nos parâmetros cosmológicos, o BINGO oferece uma oportunidade promissora para a detecção e localização de Explosões Rápidas de Rádio (FRBs). Na próxima fase do projeto, BINGO/ABDUS, serão incorporados telescópios de rádio menores em um sistema interferométrico. Propomos que os telescópios de apoio sejam baseados em uma Matriz de Abertura de Antenas Vivaldi. Simulações eletromagnéticas foram realizadas tanto para o protótipo quanto para a Estação Auxiliar com Matriz de Abertura de Antenas Vivaldi (VAAOS). A análise abrange ângulos de varredura, áreas efetivas, impacto das imprecisões na formação de feixe devido à quantização do atraso temporal, características de polarização e a emergência de lóbulos secundários em altos ângulos e frequências.

Palavras-chave: Energia Escura, Estruturas de Larca Escala do Universo, Parâmetros Cosmológicos, Instrumentação: Detectores, Telescópios

Acknowledgements

First, I would like to thank my supervisors, Prof. Dr. Elcio Abdalla, Prof. Dr. Filipe Abdalla, and Prof. Dr. David Prinsloo for their guidance in this work. I am also thankful to Dr. Alessandro Marins, Dr. Camila Novaes, and Dr. Michel Arts for some valuable discussions.

I am most of all thankful to my parents, Evelyn and Augusto, and my fiancee, Celeste, for their love and unconditional support.

This study was financed in part by the Coordenação de Aperfeiçoamento de Pessoal de Nível Superior - Brasil (CAPES) - Finance Code 001. This study was funded, in part, by the São Paulo Research Foundation (FAPESP), Brazil. Process Number 2021/08846-2 and 2023/07728-1.

Contents

Abstract	1
Resumo	2
Acknowledgements	3
List of Abbreviations	6
1 Introduction	8
1.1 Structure of this thesis	10
2 Cosmology from HI	11
2.1 The C_ℓ of the HI brightness temperature	12
2.1.1 Redshift space distortion	13
2.1.2 Partial sky: mixing matrix convolution	14
2.2 BINGO simulations	15
2.2.1 Cosmological signal.	16
2.2.2 Foreground signals.	16
2.2.3 Instrumental effects and sky coverage.	17
2.2.4 Foreground cleaning.	17
2.3 APS measurements from maps	18
2.4 Covariance Matrix	22
2.5 Likelihood and sampling methods	22
2.5.1 Priors	25
2.5.2 Multipole selection	25
2.5.3 Likelihood	26
2.5.4 Sampling	27
2.6 Results	28
2.6.1 BINGO Λ CDM constraints: exploring the systematic effects on the posterior	29

2.6.2	BINGO + Planck 2018 Λ CDM constraints: exploring the systematic effects on the posterior	31
2.6.3	BINGO Λ CDM constraints: Comparison between different realizations	33
2.6.4	BINGO + Planck Λ CDM constraints: Comparison between different realizations	33
2.7	Conclusions	36
2.8	Next steps	36
3	ABDUS project - Implementing outrigger stations with aperture arrays	38
3.1	Phased array antennas	39
3.1.1	Scanning the array	40
3.1.2	Array factors	40
3.1.3	Grating lobes	41
3.2	The technology	41
3.2.1	Beamforming	44
3.2.2	True-time delay	44
3.2.3	Vivaldi Antenna design	45
3.3	Science requirements	45
3.4	Simulated results	46
3.4.1	Tile simulation	47
	Polarization	47
	Effect of delay quantization	48
3.4.2	Outrigger station simulations	48
	Stations with randomly spaced tiles	54
	Scan angle and effective area	55
	Scan angle and grating lobes	55
3.5	Conclusions	61
4	Final remarks	62
	Bibliography	64

List of Abbreviations

2MASS	Two Micron All Sky Survey
AA	Aperture Array
ABDUS	Advanced BAO Dark Universe Studies
AF	Array Factor
APERTIF	APERture Tile In Focus
APS	Angular Power Spectrum
ASIC	Application-Specific Integrated Circuit
BAO	Baryon Acoustic Oscillations
BINGO	Baryon Acoustic Oscillations from Integrated Neutral Gas Observation
BIS	BINGO/ABDUS Interferometry System
BOSS	Baryon Oscillation Spectroscopy Survey
CDM	Cold Dark Matter
CHIME	Canadian Hydrogen Intensity Mapping Experiment
CLASS	Cosmic Linear Anisotropy Solving System
CMB	Cosmic Microwave Background
CNB	Cosmic Neutrino Background
DE	Dark Energy
DES	Dark Energy Survey
DM	Dark Matter
EFE	Einstein Field Equations
EM	Electromagnetism/Electromagnetic
EMBRACE	Electronic Multibeam Radio Astronomy Concept
FoV	Field-of-View
FAST	Five-hundred-meter Aperture Spherical Telescope
FLASK	Full-sky Lognormal Astro-fields Simulation Kit
FRB	Fast Radio Bursts
FWHM	Full Width at Half Maximum
GNILC	Generalized Needlet Internal Linear Combination

HEALPix	Hierarchical Equal Area isoLatitude Pixelation
HFSS	High-Frequency Structure Simulator
HI	Neutral Hydrogen
IM	Intensity Mapping
LNA	Low-Noise Amplifier
LOFAR	LOw Frequency ARray
LSS	Large Scale Structure
MCMC	Monte Carlo Markov Chain
MFAA	SKA Mid-Frequency Aperture Array
MWA	Murchison Widefield Array
PA	Phased Array
PS	Phase Shifters
PSM	Planck-Sky Model
RF	Radio Frequency
RFI	Radio-Frequency Interference
RMS	Root Mean Square
RSD	Redshift Space Distortion
SDSS	Sloan Digital Sky Survey
SKA	Square Kilometre Array
THEA	Thousand Element Array
TTD	True-Time Delay
UCLCL	Unified Cosmological Library for C_ℓ
VAAOS	Vivaldi Aperture Array Outrigger Station
VIMOS	VIisible MultiObject Spectrograph
VIPERS	VIMOS Public Extragalactic Redshift Survey
VNA	Vector Network Analyzer
WMAP	Wilkinson Microwave Anisotropy Probe

Chapter 1

Introduction

The study of the large-scale structure (LSS) of the universe — the spatial distribution of matter on cosmological scales — provides critical insights into the nature of dark matter and dark energy, the two main, unknown components of the Universe. The observed “cosmic web,” a vast network of galaxies, clusters, and voids, is thought to have evolved from primordial density fluctuations in the early universe. These initial fluctuations, amplified by gravitational instability, gave rise to the intricate structures observed today. The evolution of these density fluctuations, which are seeded by dark matter, depends on the properties of dark energy, as it governs the rate of cosmic expansion.

To investigate the LSS, cosmologists rely heavily on galaxy surveys that map the spatial distribution of galaxies across the observable universe. By measuring redshifts, which act as proxies for distances, these surveys capture the three-dimensional arrangement of galaxies, thus tracing the distribution of dark matter. For instance, the Sloan Digital Sky Survey (SDSS; York et al., 2000; Anderson et al., 2012; Alam et al., 2017) and its Baryon Oscillation Spectroscopic Survey (BOSS; Ross et al., 2012) follow-up have provided extensive maps that reveal the influence of dark matter and dark energy on large-scale structure (Eisenstein et al., 2005; Dawson et al., 2012).

An alternative to traditional galaxy redshift surveys is the technique of intensity mapping (IM), particularly 21-cm intensity mapping, which uses neutral hydrogen (HI) emission as a tracer of matter. Instead of cataloging individual galaxies, IM aggregates signals from many galaxies within a beam, allowing cosmologists to study vast cosmic volumes efficiently. This approach has two main advantages over galaxy surveys: i) it enables quicker surveying of larger volumes of the Universe in a shorter time, and ii) redshift can be measured directly from the redshifted 21-cm line, offering a straightforward means of mapping cosmic evolution tomographically, proving a 3D description of the LSS. IM experiments like the Baryon Acoustic Oscillations from Integrated Neutral Gas Observations (BINGO; Abdalla et al., 2022a) aims to detect BAO in the radio band using this method.

Despite its promise, HI intensity mapping faces significant challenges, primarily due to contamination from foreground emissions. At frequencies near 1 GHz, the faint HI signal ($T \approx 1$ mK) is masked by much stronger foreground emissions, such as Galactic synchrotron radiation and extragalactic point sources, which can reach intensities around $T \approx 10$ K. Advanced foreground removal techniques used in CMB analysis (Remazeilles, Delabrouille and Cardoso, 2011a) are also applied in HI data and has been employed for BINGO data (Fornazier et al., 2022). In addition to foreground challenges, instrumental systematic effects - such as 1/f noise -, beam resolution and their chromatic and shape can obscure signals on small scales, complicating data analysis. Addressing these systematics is vital for the success of HI IM experiments.

Multiple current and upcoming experiments utilize the 21-cm IM technique to map BAO, including the Canadian Hydrogen Intensity Mapping Experiment (CHIME; Bandura et al., 2014), the Five-hundred-meter Aperture Spherical Radio Telescope (FAST; Nan et al., 2011), the Square Kilometre Array (SKA; Santos et al., 2015), and Tianlai (Chen, 2012). BINGO joins this effort with a specific focus on detecting BAO at low redshifts to gain deeper insights into dark energy's influence on large-scale structures and the expansion history of the universe. BINGO's unique design includes a 40-meter primary reflector in a crossed-Dragone configuration, with 28 receiver horns for high sensitivity over a broad sky area (Abdalla et al., 2022b). Located in northeastern Brazil, BINGO's position and design allow it to observe with minimal interference, contributing valuable data on BAO.

Looking forward, the Advanced BAO and Dark Universe Studies (ABDUS; Abdalla et al., 2023) project proposes to expand BINGO's capabilities with phased-array stations, enhancing its resolution and enabling it to explore new scientific frontiers, including the detection and localization astrophysical (radio transient) sources as fast radio bursts (FRBs). FRBs are energetic, short-lived radio transients that offer additional opportunities to probe cosmic structure and refine cosmological parameters (e.g.: Walters et al., 2018; Zhao et al., 2020). With ABDUS, BINGO's sensitivity will increase through the addition of outrigger stations placed approximately 20 km from the main telescope, forming an interferometric array for high-resolution, multi-beam observations. This setup would leverage Vivaldi Aperture Array Outrigger Stations (VAAOS), based on SKA's mid-frequency prototypes (Ruiter et al., 2016), to cover frequencies from 0.5 GHz to 1.5 GHz and produce multiple beams with advanced beamforming technology.

Analyzing data from these surveys requires robust statistical tools, particularly 2-point statistics, which measure correlations in density or temperature fluctuations across different scales. In galaxy surveys, the angular power spectrum, a 2-point correlator in harmonic space, is frequently used to characterize fluctuations in projected density fields. In this study, the angular power spectrum of the 21cm signal, projected across thin redshift bins corresponding to the

BINGO channels, is analyzed to probe cosmological parameters. Theoretical predictions, derived from solutions to the Einstein-Boltzmann equations, are compared with observations, requiring the application of sophisticated statistical methods, such as Monte Carlo simulations, to constrain models.

1.1 Structure of this thesis

Chapter 2 employs Bayesian inference to simulate HI intensity mapping (IM) signals, incorporating systematic effects such as foreground residuals, thermal noise, and limitations due to beam resolution. This methodology allows for precise constraints on six Λ CDM cosmological parameters, with further improvements achieved by combining BINGO data with Planck 2018 observations. The simulations include the cosmological 21-cm signal, modeled as a multivariate lognormal distribution, along with key foreground sources relevant to the BINGO frequency range, instrumental noise, and the impact of a fixed instrumental beam resolution. Using the angular power spectrum (APS) formalism, we apply a standard Bayesian analysis framework to derive constraints from both BINGO and the combined BINGO + Planck 2018 datasets.

In *Chapter 3*, we propose an integration of BINGO/ABDUS with smaller outrigger radio telescopes, specifically through the Vivaldi Aperture Array Outrigger Station (VAAOS). Electromagnetic simulations are conducted for both the prototype tile and the potential outrigger stations. The analysis covers aspects such as scan angles, effective areas, the impact of beam-forming inaccuracies caused by time-delay quantization, polarization effects, and the formation of grating lobes at high angles and frequencies. Finally, our conclusions and final remarks are given in *Chapter 4*.

Chapter 2

Cosmology from HI

Large-scale structure (LSS) studies commonly rely on galaxy redshift surveys. Another approach, Intensity Mapping (IM), is cost-effective and efficient, measuring combined fluxes from galaxies rather than individual galaxies, with IM using neutral hydrogen (HI) as a matter tracer. IM has two key benefits: it can quickly survey large volumes and provides direct redshift measurements from the 21-cm line. BINGO is one experiment designed to measure Baryon Acoustic Oscillations (BAO) in the radio band using this technique.

However, HI IM faces challenges, notably astrophysical foregrounds like Galactic synchrotron and extragalactic sources, which have signals about 10,000 times stronger than the target HI emission. Effective foreground removal, like the GNILC method used by the Planck mission(Remazeilles, Delabrouille and Cardoso, 2011a), and careful treatment of instrumental noise is critical. BINGO employs GNILC and other methods for these tasks (Fornazier et al., 2022).

Several other telescopes, including CHIME (Bandura et al., 2014), FAST (Nan et al., 2011), SKA (Santos et al., 2015), and Tianlai (Wu et al., 2021), are also employing IM to measure BAO via the 21-cm line. BINGO aims to use HI IM to precisely constrain late-time cosmological parameters.

This chapter details constraints on cosmological parameters from HI IM simulations for BINGO’s Phase 1. These simulations include the cosmological 21-cm signal, primary foreground sources, instrumental noise, and beam resolution effects. We use the angular power spectrum (APS) with Bayesian analysis to derive constraints for BINGO and BINGO + Planck 2018 TT,TE,EE+lowE+lensing.

2.1 The C_ℓ of the HI brightness temperature

In intensity mapping experiments, the brightness temperature of the HI line is used to study the large-scale structure of the Universe. Such emission results from a transition between two energy levels of the hydrogen atom, corresponding to the hyperfine structure. The emission in the rest frame has a wavelength of 21-cm and the corresponding frequency of $\nu_{10} = 1420$ MHz. Following Marins et al., 2022, the observed (average) 21-cm brightness temperature at low-redshifts, $z < 2$, is

$$\bar{T}_{\text{HI}}(z) = \left(\frac{9\hbar c^3 A_{10}}{128\pi G k_B \nu_{10} m_{\text{HI}}} \right) \frac{\Omega_{\text{HI}}(z)}{(1+z)^2} \frac{H_0^2}{||dv/d\chi||}, \quad (2.1)$$

where H_0 is the Hubble constant and $||dv/d\chi||$ is the gradient of the specific velocity field along the line of sight and $\Omega_{\text{HI}}(z)$ is the density parameter of HI. G , c , k_B , and \hbar are the gravitational constant, speed of light, Boltzmann constant, and reduced Planck constant, respectively. A_{10} represents the spontaneous emission coefficient of the 21-cm transition, and m_{HI} is the HI atom mass. Following Battye et al., 2013; Hall, Bonvin and Challinor, 2013, this expression gets simplified by referring to the cosmic background evolution, where we can express the gradient of the specific velocity only in terms of Hubble flow

$$||dv/d\chi|| = \frac{H(z)}{(1+z)^4}, \quad . \quad (2.2)$$

Replacing the values of the fundamental constants, we find

$$\bar{T}_{\text{HI}}(z) = 188h \Omega_{\text{HI}}(z) \frac{(1+z)^2}{E(z)} \text{ mK}, \quad (2.3)$$

where $H_0 = 100 h \text{ km s}^{-1}\text{Mpc}^{-1}$ and $E(z) = H(z)/H_0$.

Like the dark matter distribution, the brightness temperature is not homogeneously distributed, and by considering its spatial anisotropy, $\Delta T_{\text{HI}}(z, \hat{n})$, we depict the temperature field as $T_{\text{HI}}(z, \hat{n}) = \bar{T}_{\text{HI}}(z) + \Delta T_{\text{HI}}(z, \hat{n})$, where \hat{n} is the unit vector along the line of sight (LoS). The temperature fluctuation ΔT_{HI} results from various mechanisms during the cosmic evolution, including the foremost contribution from the HI overdensity δ_{HI} , and approximately we have $\Delta T_{\text{HI}} = \bar{T}_{\text{HI}} \delta_{\text{HI}}$.

Since 21-cm IM surveys the Universe within tomographic redshift bins (or equivalently, frequency bins), the observable in practice is a projection of the 3D temperature field along

LoS, such that the integrated temperature fluctuation reads

$$\delta T_{\text{HI}}(\hat{n}) = \int dz \phi(z) \bar{T}_{\text{HI}}(z) \delta_{\text{HI}}(z, \hat{n}), \quad (2.4)$$

where $\phi(z)$ is the window function determining the bin width. Assuming a top-hat filter, we have $\phi(z) = 1/(z_{\max} - z_{\min})$ for $z_{\min} < z < z_{\max}$ and $\phi(z) = 0$ outside the redshift bin (Battye et al., 2013).

Following Novaes et al., 2022, the resulting Angular Power Spectrum (APS) $C_{\ell}^{ij} = \langle a_{\ell m}^i a_{\ell m}^{j*} \rangle$ for the projected HI brightness temperature is

$$C_{\ell}^{ij} = \frac{2}{\pi} \int dk W_{\text{HI},\ell}^i(k) W_{\text{HI},\ell}^j(k) k^2 P(k). \quad (2.5)$$

where the indices i, j denote tomographic redshift bins such that, for $i = j$ and $i \neq j$ we obtain auto- and cross-APS, respectively. The $W_{\text{HI},\ell}^i$ term is a window function collecting all the redshift dependencies

$$W_{\text{HI},\ell}^i(k) = \int dz b_{\text{HI}}(z) \phi(z) \bar{T}_{\text{HI}}(z) D(z) j_{\ell}(k \chi(z)), \quad (2.6)$$

where $D(z)$ is the growth function, $b_{\text{HI}}(z)$ is the HI bias as a function of the redshift, and j_{ℓ} is the spherical Bessel function. Equation (2.6) depends on two parameters of the HI astrophysics, $b_{\text{HI}}(z)$ and $\Omega_{\text{HI}}(z)$ (through Eq. (2.3)). For simplicity, we assume that the redshift bins are sufficiently thin, such that both parameters can be assumed to have constant values inside each bin. We also assume them to be scale-independent.

In our work, we use the UCLC1 code (McLeod, Balan and Abdalla, 2017; Loureiro et al., 2019), a library for calculating the angular power spectrum of the cosmological fields. Such code obtains the primordial power spectra and transfer functions from the CLASS Boltzmann code (Blas, Lesgourges and Tram, 2011) and applies Eq. 2.5 to obtain the APS. In the UCLC1, the C_{ℓ} computation may be extended some way into the non-linear regime by introducing the scale-dependent non-linear overdensity $\delta_{NL}(k, \chi)$ from the CLASS code (Blas, Lesgourges and Tram, 2011; Di Dio et al., 2013), using the modified HALOFIT of Takahashi et al., 2012. See Loureiro et al., 2019 for details.

2.1.1 Redshift space distortion

Galaxies have peculiar velocities relative to the Universe's overall expansion, creating the phenomenon of redshift space distortion (RSD). This effect causes galaxies moving towards us to

appear closer, with lower redshifts, while those moving away seem further, with higher redshifts. The RSD effect, first described by Kaiser, 1987, is accounted for in the UCLC1 code. In this work, we adapt the formalism of Fisher, Scharf and Lahav, 1994 and Padmanabhan et al., 2007, originally developed for galaxy probes, to the intensity mapping window function. Assuming peculiar velocities are small compared to the redshift slice thickness, the brightness temperature \bar{T}_{HI} is expressed as a function of redshift distance, expanded to first order to include a velocity-dependent correction.

This correction modifies the window function to include an RSD contribution, $W_{\text{RSD},\ell}^i$, alongside the standard term, $W_{\text{HI},\ell}^i$. The RSD contribution depends on the redshift distortion parameter β^i , derived from the growth rate of structure and bias of the HI tracer. The formulation neglects the Fingers of God effect, which dominates small scales due to the virial motions of galaxies in clusters (Kang et al., 2002). This refined window function enables a more accurate modeling of RSD in intensity mapping analyses.

2.1.2 Partial sky: mixing matrix convolution

The modeling given by Eq. (2.5) assumes the (brightness) temperature as an isotropic random field defined in the whole sphere. However, for comparison with the data, we need to take into account that we only survey a portion of the sky. The angular mask function $W(\hat{\mathbf{n}})$ can be expanded into spherical harmonics coefficients $w_{\ell m} = \int d\hat{\mathbf{n}} W(\hat{\mathbf{n}}) Y_{\ell m}^*(\hat{\mathbf{n}})$ and with a power spectrum

$$\mathcal{W}_\ell = \frac{1}{2\ell + 1} \sum_m |w_{\ell m}|^2. \quad (2.7)$$

Following Hivon et al., 2002 and Blake et al., 2007, the effect of the angular mask function on the power spectrum is given by a convolution with a coupling kernel

$$S_\ell = \sum_{\ell'} R_{\ell\ell'} C_{\ell'}, \quad (2.8)$$

where $R_{\ell\ell'}$, named mixing matrix, is given by

$$R_{\ell\ell'} = \frac{(2\ell' + 1)}{4\pi f_{sky}} \sum_{\ell''} \mathcal{W}_{\ell''} \begin{pmatrix} \ell & \ell' & \ell'' \\ 0 & 0 & 0 \end{pmatrix}^2. \quad (2.9)$$

The mixing matrix depends only on the mask function given by its angular power spectrum \mathcal{W}_ℓ . The 2×3 matrix above is the Wigner $3j$ function; these coefficients were calculated using the

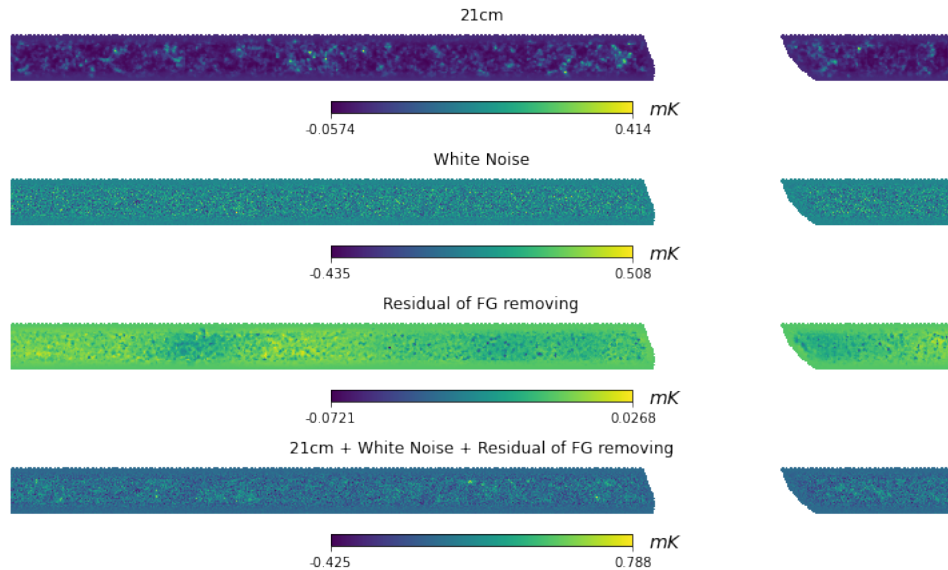


FIGURE 2.1: From top to bottom, each panel shows the pure 21-cm cosmological signal generated with the FLASK code (subsection 2.2.1, a realization of the white noise contribution (subsection 2.2.3), the residual of the foreground removing process (subsection 2.2.4), and the sum of the three components above, respectively, also accounting for the $\theta_{\text{FWHM}} = 40$ arcmin beam effect.

UCLWig 3j library¹, which optimises the calculation of Wigner $3j$ symbols using the recurrence relation by Schulten and Gordon, 1976.

2.2 BINGO simulations

The simulations used in our analyses were generated following the same procedure detailed in Novaes et al., 2022. These simulations include the cosmological 21-cm signal, the main foreground sources contributing to the BINGO frequency range, the instrumental noise, as well as the effect introduced by a fixed instrumental beam resolution. All simulations are generated in the HEALPix pixelization scheme (Gorski et al., 2005a), with the resolution of $N_{\text{side}} = 256$. We generate 500 realizations of the 21-cm signal and add to each of them the instrumental effects and the expected foreground residual contribution, which we refer to as *BINGO simulations*. Figure 2.1 shows an illustrative example of each component individually and one complete BINGO simulation. One of the simulations, picked at random, is assumed as the observation in our cosmological analysis. All the 500 BINGO simulations are used for the computation of the covariance matrix. Details of how the simulations are built are described below.

¹<https://github.com/LorneWhiteway/UCLWig3j>

2.2.1 Cosmological signal.

We used the publicly available FLASK² code (Xavier, Abdalla and Joachimi, 2016) to produce two-dimensional tomographic realizations (spherical shells around the observer, positioned at the center) of random astrophysical fields following a multivariate lognormal distribution, reproducing the desired cross-correlations between them. The lognormal distribution is more suitable to describe matter tracers than the Gaussian distribution, avoiding non-physical ($\delta < -1$) densities. FLASK takes as input the auto- and cross- C_ℓ^{ij} ($i = j$ and $i \neq j$, respectively) previously calculated for each of the i, j redshift slices.

The 21 cm C_ℓ^{ij} are computed with the UCLC1 code using the Planck 2018 Λ CDM fiducial cosmology ($(\Omega_b, \Omega_c, h, n_s, \ln 10^{10} A_s, \tau_r) = (0.0493, 0.2645, 0.6736, 0.9649, 3.044, 0.0544)$; Aghanim et al., 2020b) and HI parameters given by $\Omega_{\text{HI}} = 3.6 \times 10^{-4}$ (Padmanabhan, Choudhury and Refregier, 2015) and $b_{\text{HI}} = 1$. From them, we generated 500 lognormal realizations, each of them corresponding to 30 HEALPi \times full sky maps of 21 cm brightness temperature fluctuations, one for each BINGO frequency (or redshift) bin. For simplicity, and following some of the previous works of the BINGO collaboration (Zhang et al., 2022; Fornazier et al., 2022), we fix the number of channels at 30 ($\delta\nu = 9.33$ MHz). The impact of different tomographic binning for the cosmological analyses will be evaluated in the future (see Mericia et al., 2022, for analyses evaluating the impact of the number of redshift bins in the foreground cleaning process).

2.2.2 Foreground signals.

Using the Planck Sky Model software (PSM; Delabrouille et al., 2013), we simulate the foreground signal contributing in each frequency bin of the BINGO channels. Following Novaes et al., 2022 and Mericia et al., 2022, we consider the contribution of seven foreground components. From our Galaxy, we account for the synchrotron and free-free emissions, which are the most important contaminants in the BINGO band, as well as the thermal dust and anomalous microwave emissions. Among the extragalactic components, we include the thermal and kinetic Sunyaev-Zel'dovich effects and the unresolved radio point sources. For a detailed description of the specific configuration adopted in the PSM code to simulate each foreground component, we refer the reader to Mericia et al., 2022.

²<http://www.astro.iag.usp.br/~flask/>

2.2.3 Instrumental effects and sky coverage.

After adding the foreground contribution to a 21 cm mock, the effect of the BINGO beam is introduced to all frequency maps as being Gaussian and having the same full-width half maximum of $\theta_{\text{FWHM}} = 40 \text{ arcmin}$. We then add to the simulations the contribution of thermal (white) noise, taking into account the BINGO specifications(Wuensche et al., 2022; Abdalla et al., 2022b).

We assume BINGO phase 1 operation, with a temperature system $T_{\text{sys}} = 70 \text{ K}$, operating with 28 horns and optical arrangement as designed in Abdalla et al., 2022b, and considering 5 years of observation. To allow for a more homogeneous coverage of the BINGO region, the horns will have their positions shifted by a fraction of beam width in elevation each year. Taking these specifications into account, the thermal noise level, or the root mean square (RMS) value, by pixel, at the resolution of $N_{\text{side}} = 256$, is estimated as described in Fornazier et al., 2022. From this RMS map, we are able to generate an arbitrary number of noise realizations by multiplying it by Gaussian distributions of zero mean and unitary variance.

In order to reproduce BINGO sky coverage, we also applied a cut sky mask to the simulations. In addition to selecting the BINGO area, this mask also cuts out the 20% brightest sky pixels of the Galactic region.

2.2.4 Foreground cleaning.

To remove the contribution of the Galactic and extragalactic foreground signals, we used the Generalized Needlet Internal Linear Combination (GNILC; Remazeilles, Delabrouille and Cardoso, 2011b; Olivari, Remazeilles and Dickinson, 2016), a non-parametric technique that has been shown to perform very well over the BINGO simulations (Licciano et al., 2022; Fornazier et al., 2022; Marins et al., 2022; Mericia et al., 2022).

GNILC is a blind method; that is, no information on the foreground signal is used, and it relies on the fact that the foregrounds are significantly more correlated among the frequency channels than the 21-cm signal. It uses prior knowledge of the 21-cm IM signal along with the thermal noise signal, the APS, to evaluate the local ratio between the 21-cm plus noise and the total observed signal, then used to estimate the effective dimension of the 21-cm signal plus noise subspace. GNILC uses a set of needlets to decompose the observations into different angular scales for different sky positions to estimate the foreground emission contribution considering both of these parameters, working as a band-pass filter. Then, for each needlet scale, the 21-cm plus noise signal is reconstructed in the subspace orthogonal to that of the foregrounds. The cosmological signal is preserved while filtering out the foreground signal. By adding the

maps from each of the needlet scales, GNILC reconstructs the 21-cm plus noise signal maps at each frequency.

We note that the foreground cleaning process using GNILC is computationally expensive, so applying it to all 500 simulations is time-consuming. For this reason, we perform the foreground cleaning over only one complete simulation and estimate the foreground residual maps, i.e., the contamination expected to remain along with the cosmological signal in each of the redshift bins. Then, following Novaes et al., 2022, the 500 BINGO simulations are constructed by adding the realistic foreground residual contribution to the 21 cm mocks after accounting for the beam effect and adding different noise realizations to each of them.

2.3 APS measurements from maps

Given our simulated temperature fluctuation maps, let $a_{\ell m}$ be the coefficients of spherical harmonic expansion. The pseudo- C_ℓ estimate that takes into account beam resolution, pixelation scheme, and sky coverage corrections is defined by

$$\hat{S}_\ell^{ij} = \frac{1}{f_{\text{sky}} b_\ell^2 w_\ell^2} \sum_{m=-\ell}^{\ell} a_{\ell m} a_{\ell m}^* \quad (2.10)$$

Here, b_ℓ is the axisymmetric beam window function (e.g. Challinor and Lewis, 2011) assumed in this work as a Gaussian beam and w_ℓ is the pixel window function (Gorski et al., 2005b; Leistedt et al., 2013). The beam window function corrects the effect of the beam resolution on the observed angular power spectrum. It was computed assuming the beam to be Gaussian with a full-width half-maximum of $\theta_{\text{FWHM}} = 40$ arcmin. The pixel window function corrects a suppression of power on small scales caused by the effect of the finite size of the HEALpix pixel. For a detailed discussion, we refer to the HEALpix manual³.

Although Eq. 2.10 is an unbiased estimate for pure 21-cm maps, it is not unbiased when white noise is included. In order to remove the contribution from the white noise signal, we use a debiasing procedure. A similar debiasing used for BINGO analysis is described in Fornazier et al., 2022; Mericia et al., 2022. In these references, the debiasing takes into account both an additive bias due to the noise contribution and a multiplicative bias due to the estimation of GNILC of 21 cm from the foreground. Here, we only take into account additive bias. Since the foreground residuals are quite small, we are mainly concerned with the contribution of white noise. Let $\hat{S}_\ell^{ij, \text{biased}}$ be Eq. 2.10 applied to a noisy map, that is, included white noise. The

³<https://healpix.sourceforge.io/>

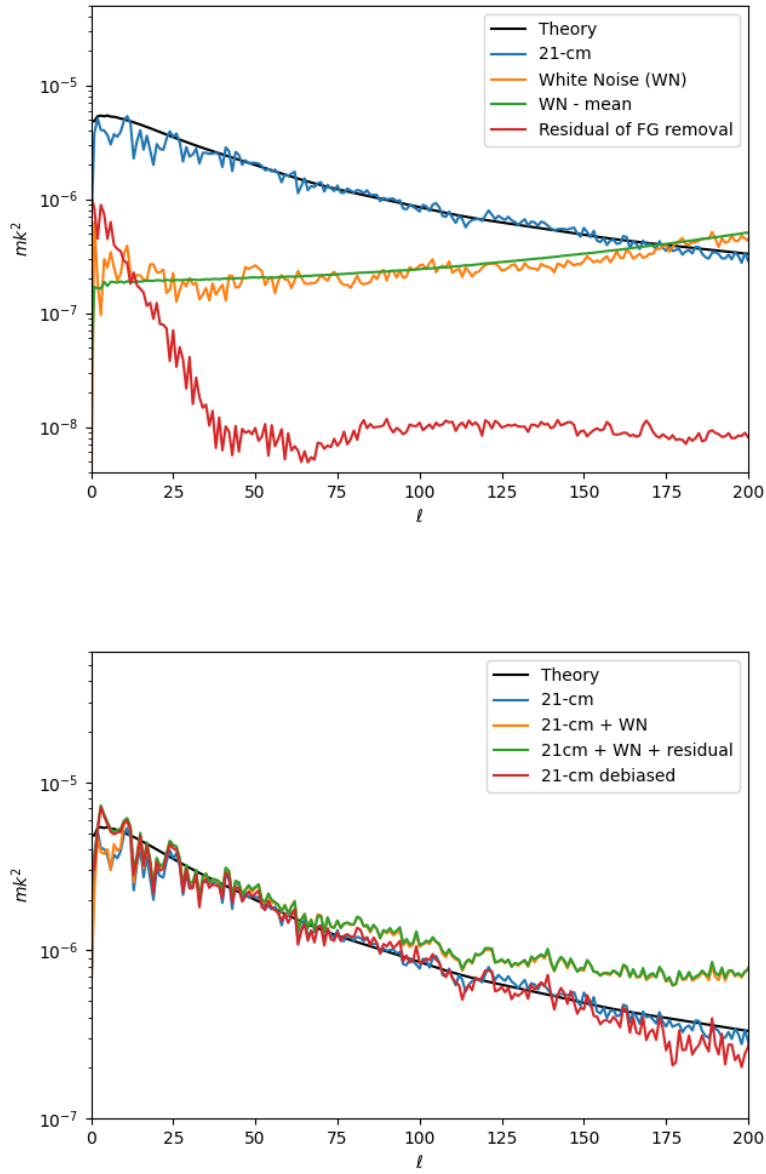


FIGURE 2.2: Top: The APS of respectively a pure 21-cm signal (blue), a noise simulation (yellow), the averaged APS from 1000 noise simulations (green), and the APS of the residual of foreground removal (red). Bottom: The APS of the pure 21-cm (blue), 21-cm added to noise (yellow), 21-cm added to noise and residual of foreground removal (green), and the debiased APS (red). The noise has higher power than the signal for high ℓ (lower scales), and this effect is corrected in the debiasing process. However, the debiasing does not correct the effect introduced by the residual of foreground removal on lower ℓ (higher scales).

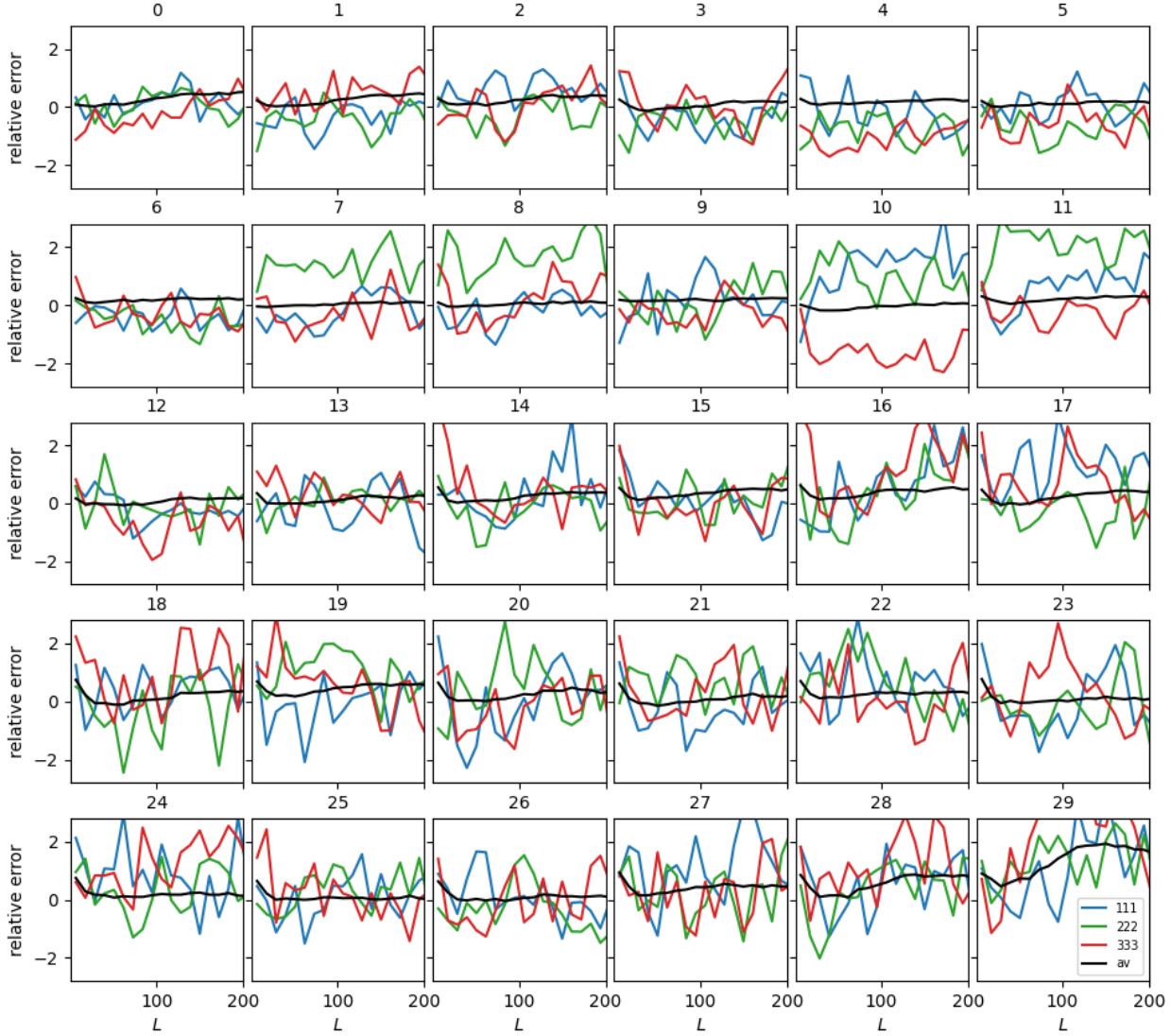


FIGURE 2.3: The blue, green, and red lines represent the relative error $(\hat{S}_L - S_L^{th})/\sigma_L^{Flask}$ computed for three different realizations of BINGO simulations. The 30 channels are defined in Table 2.2. It includes the white noise and foreground removal systematic effects. The black line is the average of the relative error for the 500 simulations. This plot shows that neighboring multipoles are highly correlated. The black line is roughly zero except for the lowest multipoles ($\ell \lesssim 25$) in all channels and the highest multipoles for some of the highest redshifts due to the systematics of foreground removal.

unbiased APS estimate is

$$\hat{S}_\ell^{ij,debiased} = \hat{S}_\ell^{ij,biased} - \langle \hat{S}_\ell^{noise} \rangle \quad (2.11)$$

where $\langle \hat{S}_\ell^{noise} \rangle$ is the average noise power spectrum for 1000 random Gaussian noise realizations as described in sec. 2.2.3, and $\hat{S}_\ell^{ij,biased}$ is the biased estimate. From now on, \hat{S}_ℓ^{ij} will always denote the debiased estimate when referring to a noisy map.

We further perform a bandwidth binning on the S_ℓ s. This binning acts on the measurement in a way that decorrelates mixed modes. We bin the ℓ values into bins $\Delta\ell$ of width 11 (so, e.g., the first bin is $2 \leq \ell \leq 12$). For each bin, we calculate a weighted average of the \hat{S}_ℓ (weighted by the number of spherical harmonic coefficients),

$$\hat{S}_L^{ij} = \frac{\sum_{\ell=\ell_0}^{\ell_0+\Delta\ell-1} (2\ell+1) \hat{S}_\ell^{ij}}{\sum_{\ell=\ell_0}^{\ell_0+\Delta\ell-1} (2\ell+1)}, \quad (2.12)$$

where ℓ_0 is the first multipole of each bin, e.g., 2, 13, 24, Here, L simply denotes each multipole bin.

Figure 2.3 illustrates the relative error $(\hat{S}_L - S_L^{th})/\sigma_L^{Flask}$, computed in relation to the UCLC1 theoretical S_L^{th} at the fiducial cosmology. This plot draws attention to the behavior of the errors for a range of multipoles with respect to both the UCLC1 theoretical spectrum and the Flask-estimated standard deviation σ_L^{Flask} .

While the average \hat{S}_L^{ij} values from the 500 simulations closely track the UCLC1 theoretical spectrum, it is evident that the random errors on the spectrum for individual realizations, i.e., cosmic variance, exhibit strong correlations among neighboring multipoles within the same redshift bin. Let us take, for example, the redshift bin 10. The realization depicted in blue and in orange shows mostly positive errors, while the realization depicted in green shows mostly negative errors within the depicted multipole range.

By examining Fig. 2.3, we can discern random errors from systematic errors. While the colored lines present both random and systematic errors, the black line only presents systematic errors, as the random errors vanish when averaged out. The black line reveals positive systematic errors in low multipoles ($\ell \lesssim 25$) across all redshift bins. These errors are primarily attributed to the process of foreground removal. A second type of systematic error manifests in high multipoles, primarily within the highest redshift bins. This phenomenon is also linked to the foreground removal process, as its influence diminishes when only white noise effects are considered.

2.4 Covariance Matrix

For cosmological inference, it's essential to quantify the uncertainties associated with the observed power spectrum. To achieve this, we calculate the covariance matrix based on a set of $N_{\text{sim}} = 500$ BINGO simulations, as elaborated upon in section 2.2. Let $\hat{S}_L^{ij,n}$ be the weighted estimation of the angular power spectrum of the BINGO n-th realization, the covariance matrix of the ensemble of angular power spectra is

$$\mathcal{C}_{LL'}^{ij} = \frac{1}{N_{\text{sim}} - 1} \sum_{n=1}^{N_{\text{sim}}} \left(\hat{S}_L^{ij,n} - \langle \hat{S}_L^{ij} \rangle \right) \left(\hat{S}_{L'}^{ij,n} - \langle \hat{S}_{L'}^{ij} \rangle \right)^T, \quad (2.13)$$

where $\langle \hat{S}_L^{ij} \rangle$ is the average pseudo- C_ℓ estimate for the 500 BINGO simulations. Figs. 2.4 and 2.5 show the Pearson correlation coefficient $\mathcal{C}_{LL'}/\sqrt{\mathcal{C}_{LL}\mathcal{C}_{L'L'}}$ computed from the FLASK covariance matrix. The degree of correlation among different multipoles can be inferred from the diagonal properties of this matrix. The figures presented illustrate the correlation characteristics of both the pure simulated 21-cm cosmological signal and the debiased signal after accounting for systematic error sources.

In both instances, the correlation decreases with the redshift, leading to matrices with more pronounced diagonal features for the highest redshift bins. However, a distinction arises when comparing the pure 21-cm signal's correlation with that of the debiased signal incorporating systematic error sources.

In the case of the pure 21-cm signal, the non-diagonal correlation intensifies for higher multipoles, a trend not mirrored in the debiased signal scenario post-inclusion of systematics. This divergence originates from the influence of white noise, which predominates over the 21-cm signal in high multipoles ($\ell \gtrsim 200$). The non-Gaussian nature of the cosmological signal introduces correlation in high multipoles, but this effect is dampened by the substantial presence of Gaussian white noise.

2.5 Likelihood and sampling methods

The Bayesian framework has been widely used in cosmology to make inferences about the parameters of cosmological models in light of data from the large-scale structure (LSS). We follow a standard Bayesian analysis framework as commonly performed in the literature (e.g. Krolewski, Ferraro and White, 2021; Contarini et al., 2022; Loureiro et al., 2019a; Köhlinger et al., 2017; Thomas, Abdalla and Lahav, 2011; Abbott et al., 2019; Blake et al., 2007).

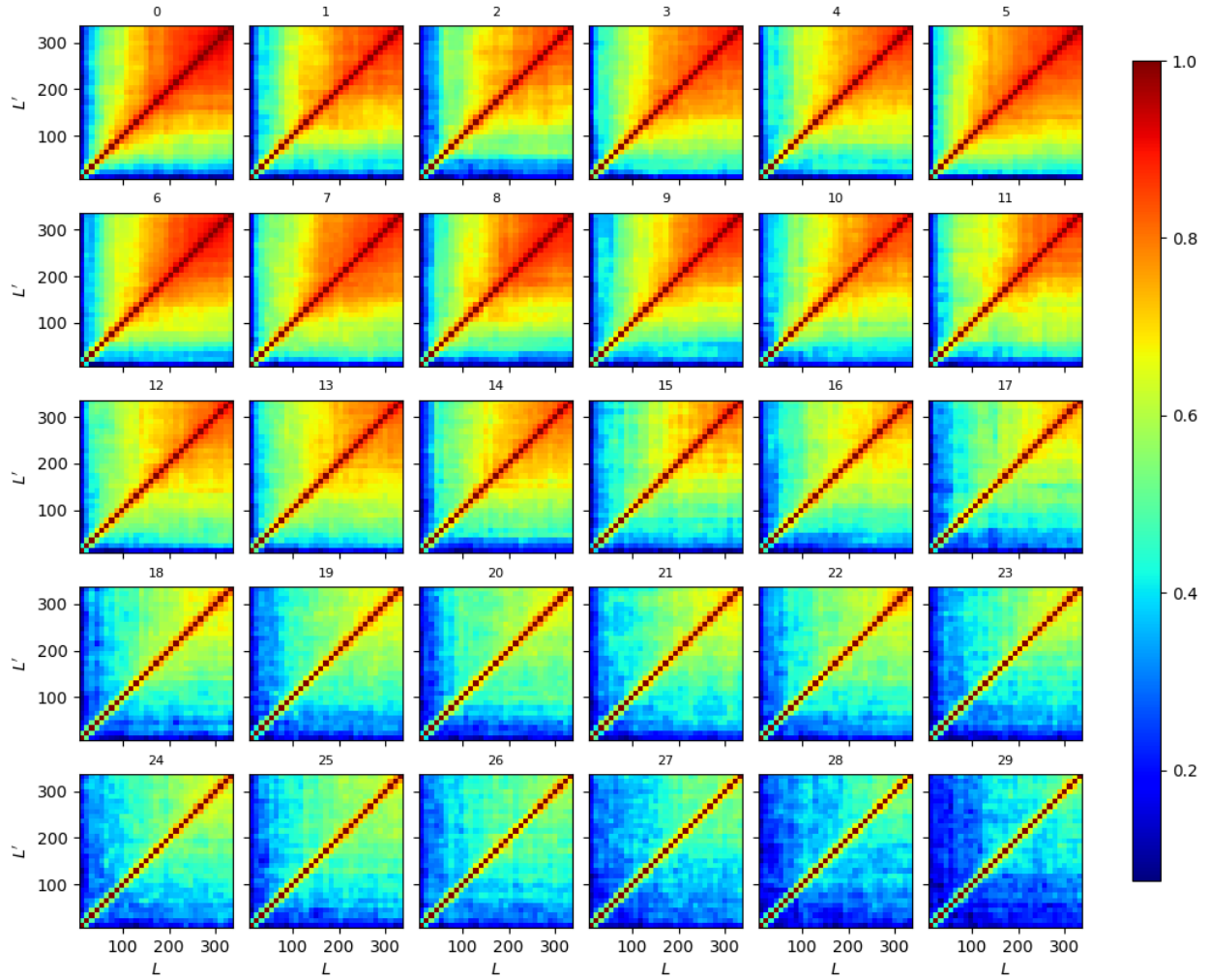


FIGURE 2.4: Pearson correlation coefficient $\mathcal{C}_{LL'}/\sqrt{\mathcal{C}_{LL}\mathcal{C}_{L'L'}}$ where $\mathcal{C}_{LL'}$ is the FLASK covariance matrix. In this plot, we did not include any systematics, so the correlation represents the pure 21-cm signal. There are two overall behaviors: the correlation increases with multipole, and the correlation decreases with redshift.

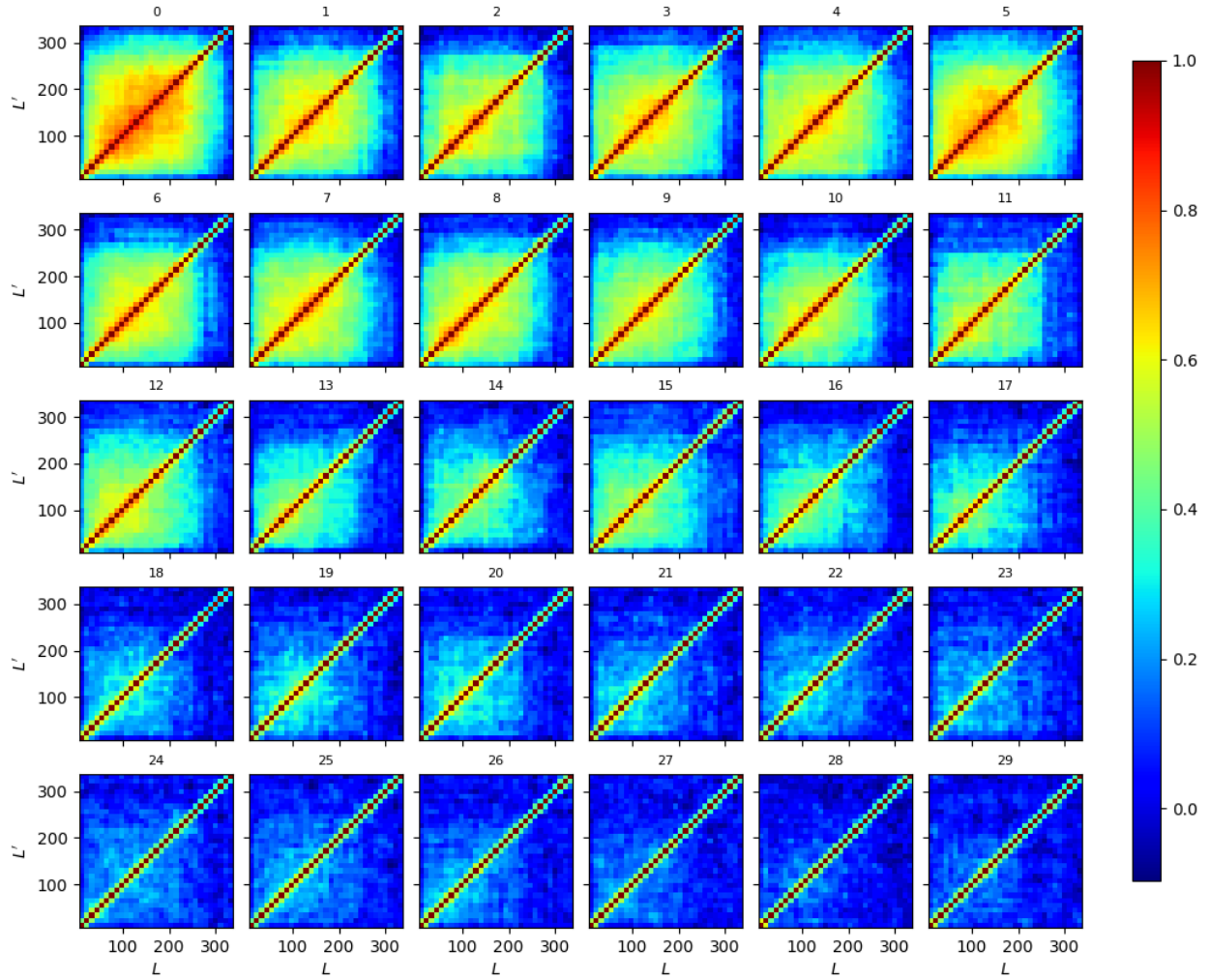


FIGURE 2.5: Pearson correlation coefficient $\mathcal{C}_{LL'}/\sqrt{\mathcal{C}_{LL}\mathcal{C}_{L'L'}}$, where $\mathcal{C}_{LL'}$ is the FLASK covariance matrix. White Nose and foreground removal systematic effects included. As in the pure 21-cm case, the correlation decreases with redshift bin. However, here, the correlation decreases for multipoles $\ell \gtrsim 200$.

TABLE 2.1: Prior ranges for the cosmological analysis. The horizontal line divides the cosmological parameters (upper part) and the nuisance parameters (lower part). τ_r is only included in the analysis that includes Planck CMB data. The index i in the nuisance parameters above indicates that they are defined for each redshift bin as independent parameters, resulting in a total of 60 independent nuisance parameters.

Parameter	Prior
Ω_b	0.03, 0.07
Ω_c	0, 0.7
h	0.5, 1
n_s	0.87, 1.07
$\ln 10^{10} A_s$	0.5, 5
τ_r	0.01, 0.2
b_{HI}^i	0.8, 1.2
$\Omega_{\text{HI}}^i b_{\text{HI}}^i$	$2 \times 10^{-4}, 6 \times 10^{-4}$

2.5.1 Priors

In this work, we take the standard approach of assuming that the priors are uniformly distributed (flat priors). Flat priors are used in order to reduce the dependence of the results on the choice of prior, allowing the data to drive the results and avoid potential biases from strong prior beliefs (Massimi, 2021; Diacoumis and Wong, 2019; Efstathiou, 2008). The prior ranges defined for our analysis are shown in Table 2.1 for all parameters considered in the cosmological analysis: the baryonic matter density (Ω_b), the cold dark matter density (Ω_c), the amplitude of the primordial power spectrum (A_s), the spectral index (n_s), the Hubble constant (h), the optical depth at reionisation epoch (τ_r), the HI bias b_{HI}^i and the HI density (Ω_{HI}^i). The nuisance parameters are assumed constant within each redshift bin and scale independent.

2.5.2 Multipole selection

While the C_ℓ discussed in Section 2.1 incorporates dark matter non-linearities, it omits non-linear effects stemming from HI physics, such as scale-dependent bias. To address this, we opted to establish cuts in ℓ_{max} for each tomographic redshift bin, a strategy aimed at excluding non-linear scales. We computed the linear and non-linear C_ℓ at fiducial cosmology (the same used in Sec 2.2.1) and performed a cut in ℓ_{max} where the percent deviation between the linear and non-linear models were smaller than 10%. Additionally, we drop out small multipoles where foreground removal systematic errors appear. We fix $\ell_{min} = 25$ for all multipoles. The

employed multipole selection, along with the bandwidth binning, yields a relatively small number of data points for the initial redshift bins. Expanding the range of ℓ_{max} could enhance the precision of the constraints. However, given the absence of a non-linear theory for HI physics, our objective is to derive realistic constraints from the linear regime. The specific ℓ_{min} and ℓ_{max} values resulting from this approach for all redshift bins are presented in Table 2.2.

Channel	Freq. (MHz)	ℓ_{min}	ℓ_{max}	Channel	Freq. (MHz)	ℓ_{min}	ℓ_{max}
0	1255.33	25	42	15	1115.33	25	97
1	1246	25	44	16	1106	25	100
2	1236.67	25	48	17	1096.67	25	106
3	1227.33	25	52	18	1087.33	25	111
4	1218	25	54	19	1078	25	114
5	1208.67	25	58	20	1068.67	25	119
6	1199.33	25	61	21	1059.33	25	125
7	1190	25	65	22	1050	25	129
8	1180.67	25	69	23	1040.67	25	135
9	1171.33	25	72	24	1031.33	25	139
10	1162	25	77	25	1022	25	145
11	1152.67	25	79	26	1012.67	25	150
12	1143.33	25	85	27	1003.33	25	155
13	1134	25	89	28	994	25	161
14	1124.67	25	93	29	984.66	25	165

TABLE 2.2: Multipole range considered for cosmological analysis. The ℓ_{max} represents the multipole in which the percent deviation between the linear and non-linear models is smaller than 10%. The ℓ_{min} was selected to exclude low multipoles with high systematic errors from the foreground removal. We also apply a bandwidth binning of $\Delta\ell = 11$. Each channel has a frequency width of 9.33MHz. The frequencies shown are the central frequency for each bin.

2.5.3 Likelihood

The likelihood quantifies the agreement between the hypothesis and the data. Following Loureiro et al., 2019, we assume the likelihood to have the Gaussian form,

$$\mathcal{L}(\Theta) = \frac{1}{\sqrt{|2\pi\mathcal{C}|}} \exp\left(-\frac{1}{2}\chi^2(\Theta)\right), \quad (2.14)$$

where

$$\chi^2(\Theta) = \left[\hat{S}_L - S_L^{th}(\Theta) \right]^T \mathcal{C}^{-1} \left[\hat{S}_L - S_L^{th}(\Theta) \right]. \quad (2.15)$$

The \hat{S}_L is the pseudo-APS estimate measured from our dataset (Sec. 2.3), $S_L^{th}(\Theta)$ is the theoretical spectrum calculated with `UCLC1` code (Sec. 2.1) after being convolved with the mixing matrix (Eq. 2.8) and being binned with the same multipole bandwidth of the data (Eq. 2.12). Finally, \mathcal{C} is the covariance matrix (Sec. 2.3) encapsulating the uncertainties and correlations between the data points.

The presented likelihood function (Eq. 2.14) is based on the assumption that the observed data follows a Gaussian distribution. This approximation, however, is somewhat coarse due to the lognormal field's inherent non-Gaussian characteristics. To explore the potential of non-Gaussian likelihoods, further investigation and testing could be pursued in future endeavors.

Tighter constraints on the cosmological parameters can be obtained by combining BINGO with the Planck 2018 dataset. Assuming that each probe provides independent information, the joint likelihood is

$$\mathcal{L}_{\text{BINGO + Planck}} = \mathcal{L}_{\text{BINGO}} \times \mathcal{L}_{\text{Planck}}. \quad (2.16)$$

The CMB data from Planck was added through the Planck likelihood codes `Commander` and `Plik` (Aghanim et al., 2020a). We include in our analysis the likelihood `lowTT` (temperature data over $2 \leq \ell \leq 30$), `Planck TT,TE,EE` (the combination of Planck TT, Planck TE, and Planck EE, taking into account correlations between the TT, TE, and EE spectra at $\ell > 29$), `lowE` (the EE power spectrum over $2 \leq \ell \leq 30$) and the Planck CMB lensing likelihood. The multiplication of these four likelihoods is commonly referred as `Planck TT,TE,EE+lowE+lensing`.

2.5.4 Sampling

Sampling points in parameter space play a crucial role in Bayesian inference, as they allow us to estimate the posterior distribution of the parameters. Some traditional MCMC methods are Metropolis–Hastings (Metropolis et al., 1953; Hastings, 1970), Gibbs sampling (Geman and Geman, n.d.), Hamiltonian sampling (Duane et al., 1987), and thermodynamic integration (Ruanaidh and Fitzgerald, 2012). In our work, we use the nested sampling method (Skilling, 2004; Skilling, 2006).

Nested sampling is more efficient than traditional MCMC methods because it uses the information about the prior volume to guide the sampling instead of randomly proposing moves in the parameter space as in Metropolis-Hastings. The algorithm works by constructing a sequence of nested sets of points in parameter space, each set being a subset of the previous one,

TABLE 2.3: Marginalised cosmological Λ CDM constraints and 68% credible intervals for BINGO simulations for the three cases: pure cosmological 21-cm signal; the cosmological signal added of white noise; the cosmological signal added of white noise and residuals of foreground removal.

Parameter	21cm	21cm+WN	21cm+WN+res
Ω_b	0.0517 ± 0.0069	$0.0509^{+0.0062}_{-0.0061}$	$0.0465^{+0.0071}_{-0.0072}$
Ω_c	0.307 ± 0.020	$0.292^{+0.022}_{-0.021}$	$0.307^{+0.022}_{-0.021}$
h	$0.716^{+0.032}_{-0.033}$	$0.748^{+0.034}_{-0.036}$	0.720 ± 0.036
n_s	0.951 ± 0.036	$0.953^{+0.034}_{-0.036}$	0.968 ± 0.035
$\ln 10^{10} A_s$	2.26 ± 0.17	$2.12^{+0.19}_{-0.18}$	2.20 ± 0.21

TABLE 2.4: Similar to Table 2.3, but for the BINGO + Planck 2018 likelihood.

Parameter	Planck	Planck + BINGO		
		21cm	21cm+WN	21cm+WN+res
Ω_b	$0.04942^{+0.00074}_{-0.00072}$	$0.05049^{+0.00034}_{-0.00031}$	$0.05034^{+0.00034}_{-0.00033}$	$0.05067^{+0.00030}_{-0.00028}$
Ω_c	0.2648 ± 0.0081	$0.2777^{+0.0034}_{-0.0035}$	$0.2754^{+0.0038}_{-0.0036}$	0.2792 ± 0.0033
h	$0.6726^{+0.0064}_{-0.0063}$	0.6627 ± 0.0025	$0.6643^{+0.0026}_{-0.0027}$	$0.6617^{+0.0023}_{-0.0024}$
n_s	0.9649 ± 0.0041	$0.9612^{+0.0018}_{-0.0020}$	$0.9612^{+0.0018}_{-0.0020}$	$0.9606^{+0.0018}_{-0.0019}$
$\ln 10^{10} A_s$	$3.043^{+0.016}_{-0.015}$	$3.0349^{+0.0080}_{-0.0087}$	$3.0371^{+0.0081}_{-0.0086}$	$3.0361^{+0.0082}_{-0.0079}$
τ_r	$0.0538^{+0.0090}_{-0.0084}$	$0.0477^{+0.0042}_{-0.0047}$	$0.0489^{+0.0044}_{-0.0045}$	0.0477 ± 0.0042

and keeping track of the points that have the highest likelihood. `Multinest` (Feroz and Hobson, 2008; Feroz, Hobson and Bridges, 2009; Feroz et al., 2013) is the most popular and freely accessible software package that implements the nested sampling method.

In this work, we employ `Pliny` (Rollins, 2015), an open-source nested sampling algorithm implementation that prioritizes optimal parallel performance on both distributed and shared memory computing clusters. `Pliny` has been successfully applied to cosmological analysis as in (McLeod, Balan and Abdalla, 2017; Loureiro et al., 2019b; Loureiro et al., 2019a; Jeffrey and Abdalla, 2019).

2.6 Results

In this section, we conducted a series of tests on the BINGO simulation within the framework of a flat Λ CDM cosmology. In subsections 2.6.1 and 2.6.2, we discuss the impact of various error sources on the accuracy of our cosmological parameter estimates. In subsections 2.6.3 and 2.6.4, we compare the parameter constraints from different realizations of the BINGO simulation. In subsection ??, the constraints on the nuisance parameters, and in subsection ??, we discuss the accuracy of the Monte Carlo fits.

TABLE 2.5: Marginalized cosmological Λ CDM constraints and 68% credible intervals for different realizations of BINGO simulation. The realizations are 111, 222 and 333. White noise and foreground removal systematic error effects are included.

Parameter	Realization 1	Realization 2	Realization 3
Ω_b	$0.0465^{+0.0071}_{-0.0072}$	$0.0451^{+0.0084}_{-0.0082}$	$0.0541^{+0.0068}_{-0.0067}$
Ω_c	$0.307^{+0.022}_{-0.021}$	$0.278^{+0.027}_{-0.024}$	$0.273^{+0.019}_{-0.018}$
h	0.720 ± 0.036	$0.754^{+0.037}_{-0.039}$	$0.725^{+0.036}_{-0.039}$
n_s	0.968 ± 0.035	$0.966^{+0.034}_{-0.033}$	$0.987^{+0.034}_{-0.033}$
$\ln 10^{10} A_s$	2.20 ± 0.21	$2.08^{+0.20}_{-0.19}$	$2.31^{+0.20}_{-0.19}$

TABLE 2.6: Similar to Table 2.3, but for the BINGO + Planck 2018 likelihood.

Parameter	Planck	Planck + BINGO		
		Realization 1	Realization 2	Realization 3
Ω_b	$0.04942^{+0.00074}_{-0.00072}$	$0.05067^{+0.00030}_{-0.00028}$	$0.05023^{+0.00034}_{-0.00033}$	$0.05016^{+0.00036}_{-0.00031}$
Ω_c	0.2648 ± 0.0081	0.2792 ± 0.0033	$0.2741^{+0.0037}_{-0.0036}$	$0.2738^{+0.0039}_{-0.0035}$
h	$0.6726^{+0.0064}_{-0.0063}$	$0.6617^{+0.0023}_{-0.0024}$	$0.6655^{+0.0025}_{-0.0027}$	$0.6654^{+0.0026}_{-0.0027}$
n_s	0.9649 ± 0.0041	$0.9606^{+0.0018}_{-0.0019}$	0.9618 ± 0.0020	$0.9624^{+0.0018}_{-0.0020}$
$\ln 10^{10} A_s$	$3.043^{+0.016}_{-0.015}$	$3.0361^{+0.0082}_{-0.0079}$	3.0345 ± 0.0083	$3.0315^{+0.0084}_{-0.0091}$
τ_r	$0.0538^{+0.0090}_{-0.0084}$	0.0477 ± 0.0042	0.0478 ± 0.0043	$0.0469^{+0.0043}_{-0.0042}$

2.6.1 BINGO Λ CDM constraints: exploring the systematic effects on the posterior

Initially, we examined the parameter fitting outcomes with sole consideration for the pure 21-cm cosmological signal. This preliminary analysis was performed using data from the BINGO simulation for pure 21-cm signals, devoid of any systematic error. Subsequently, we extended our investigation to include the influence of white noise. To achieve this, both the measured C_ℓ values, designated for fitting, and the associated covariance matrix were sourced from BINGO simulations that incorporated white noise, as elaborated upon in Section 2.2. Finally, we took into account the residual foregrounds following the methodology outlined in Section 2.2.

We probed five cosmological parameters: Ω_b , Ω_c , h , n_s , and $\ln 10^{10} A_s$, in addition to 60 nuisance parameters. The ranges of which parameter are specified in Table 2.1, and the visual representation of our findings, in the form of contour plots, can be found in Figure 2.6. The constrained parameters, along with their corresponding 68% confidence intervals, are summarized in Table 2.3. We observed that our analysis pipeline effectively constrains the Λ CDM parameters even in the presence of systematic errors. Notably, the constrained values of the Λ CDM

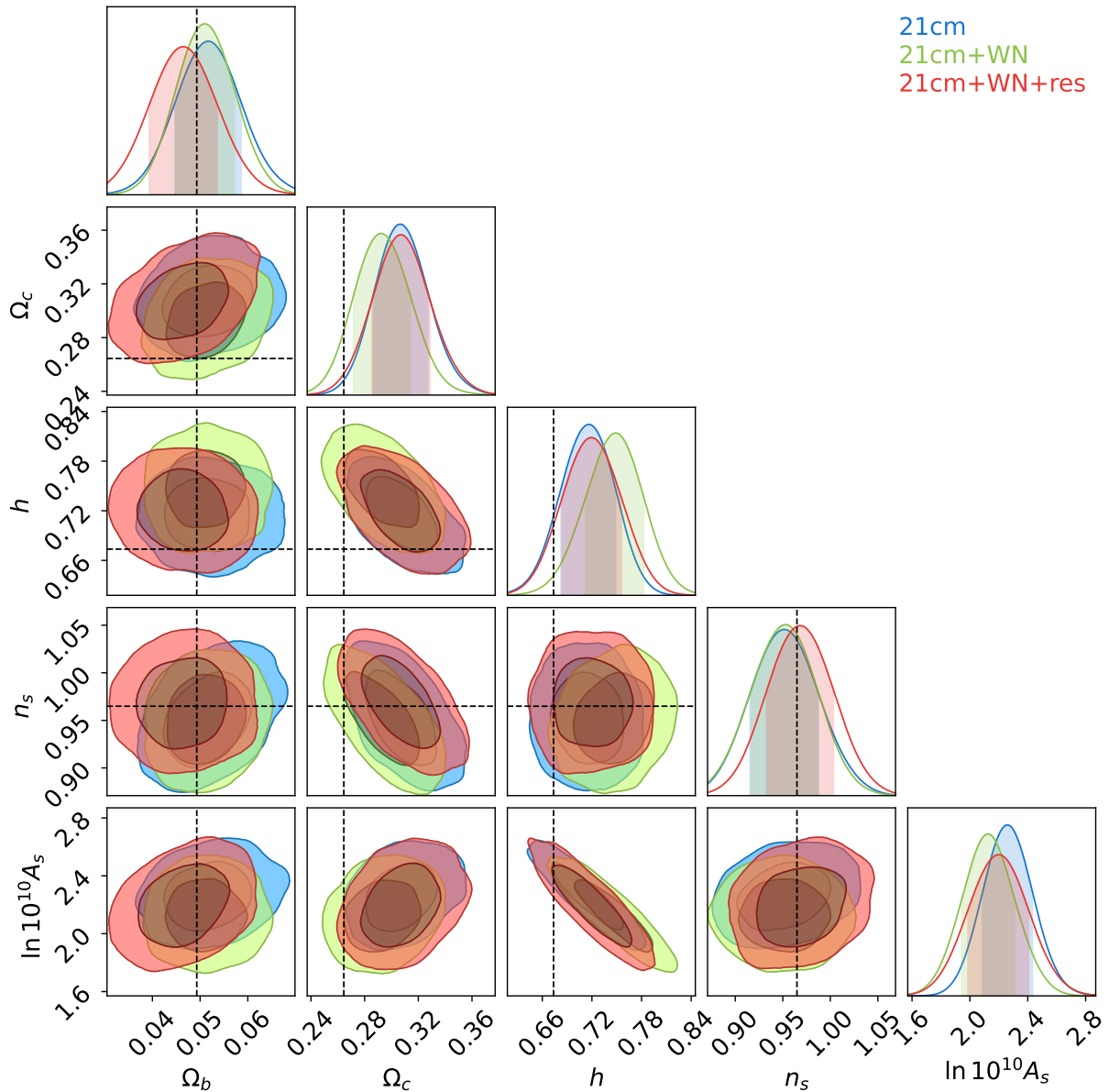


FIGURE 2.6: BINGO Λ CDM contours. The colored contour are distinguished by their sky composition for only cosmological 21-cm (blue), 21-cm and instrumental white noise (green), and a further addition of foreground residual (red).

parameters exhibited consistent behavior across the three scenarios. Furthermore, the confidence levels associated with these estimates remained similar across the different cases. This suggests that systematic error sources do not increase, as a rule, the uncertainty surrounding our parameter estimates. All the constrained parameters aligned well with the Planck 2018 fiducial cosmology within a 2σ confidence interval, except for $\ln 10^{10} A_s$. This specific parameter governs the amplitude of the power spectrum, making it inherently degenerated with the nuisance parameters $\Omega_{\text{HI}}^i b_{\text{HI}}^i$, which also dictate the amplitude of redshift bins.

2.6.2 BINGO + Planck 2018 Λ CDM constraints: exploring the systematic effects on the posterior

We calculated constraints on the cosmological parameters by combining data from BINGO simulations with the Planck 2018 likelihood. We probed six cosmological parameters: Ω_b , Ω_c , h , n_s , $\ln 10^{10} A_s$ and τ_r , in addition to the 60 nuisance parameters. Planck’s measurements offer stronger constraints compared to other independent cosmology experiments. Our aim was to assess how much the inclusion of BINGO data can enhance accuracy when both datasets are used together. The outcomes are visually depicted through probability contours in Figure 2.7. Additionally, the constrained parameter values, along with their corresponding 68% confidence intervals, can be found in Table 2.4.

Our analysis underscores that incorporating BINGO data significantly refines the precision of parameter constraints compared to relying solely on the Planck likelihood. Even when considering all systematic errors, the inclusion of BINGO significantly elevates the accuracy in determining cosmological parameters compared to relying on Planck data alone. For the simulation that includes white noise and foreground removal, we got $\Omega_b = 0.05067^{+0.00030}_{-0.00028}$, $\Omega_c = 0.2792 \pm 0.0033$, $h = 0.6617^{+0.0023}_{-0.0024}$, $n_s = 0.9606^{+0.0018}_{-0.0019}$, $\ln 10^{10} A_s = 3.0361^{+0.0082}_{-0.0079}$, $\tau_r = 0.0477 \pm 0.0042$. This corresponds to a decrease on the confidence level with respect to the Planck-only one by 60.27% for Ω_b , 59.26% for Ω_c and 62.99% for h .

Moreover, the Planck 2018 dataset effectively untangles the degeneracies between $\ln 10^{10} A_s$ and $\Omega_{\text{HI}}^i b_{\text{HI}}^i$, resulting in all constrained cosmological parameters, including $\ln 10^{10} A_s$, aligning with Planck 2018 cosmology within a 2σ confidence level. The probability contours in the combined BINGO + Planck analysis across the three distinct scenarios examined in this study consistently present congruent constrained parameter values and confidence intervals. This behavior confirms our earlier observation in the BINGO-only study: the inclusion of systematic error sources does not systematically increase the level of uncertainty linked to the cosmological parameters.

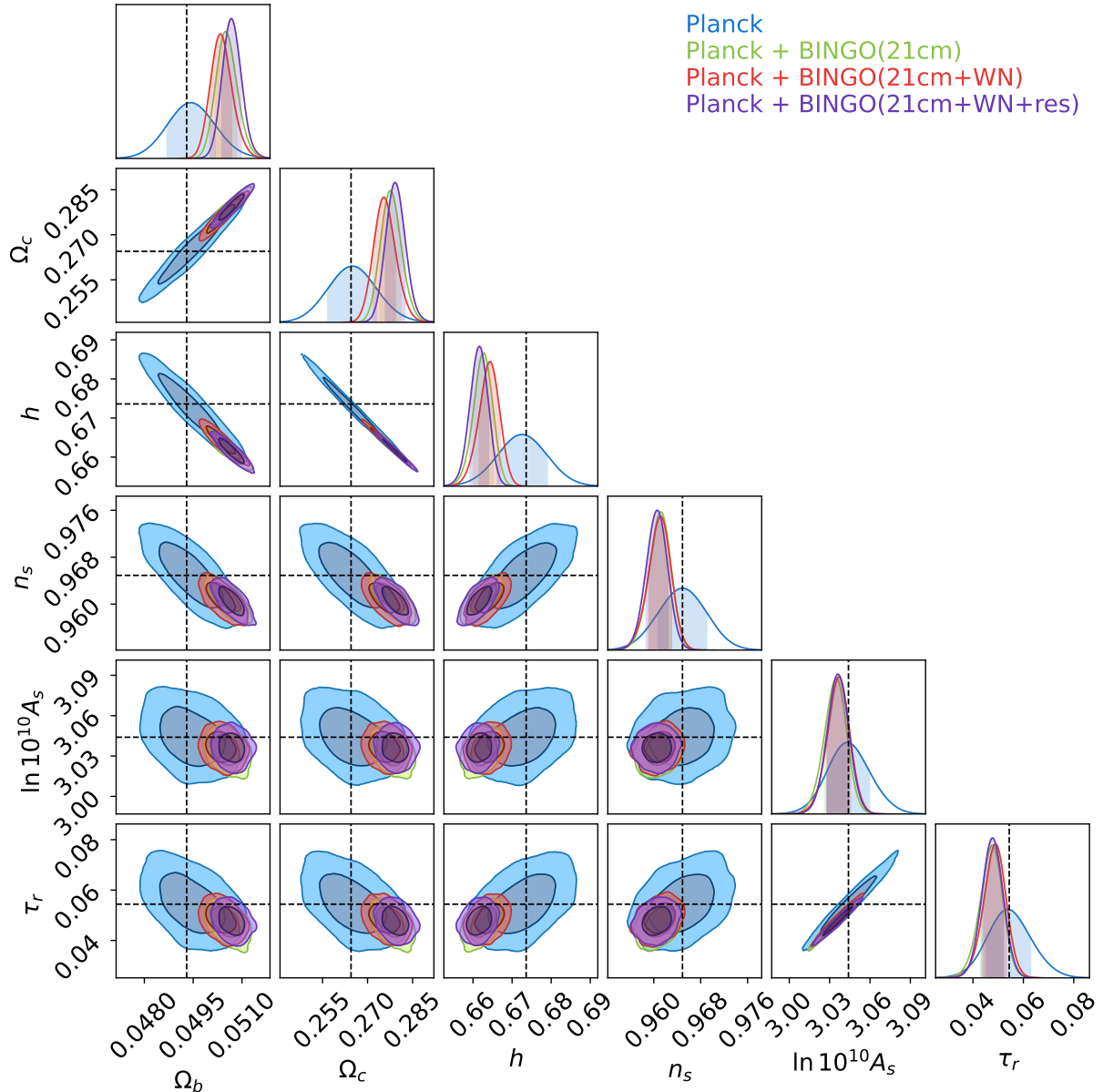


FIGURE 2.7: The blue contour represents the posterior from Planck 2018 data while the others BINGO + Planck 2018 Λ CDM contours. The green contour were computed for a BINGO simulation that only included the cosmological 21-cm signal, the red contour assumed the same 21-cm realization but included white noise, and the purple contour also included residual foreground removal.

2.6.3 BINGO Λ CDM constraints: Comparison between different realizations

We have established that the data is characterized by pronounced, correlated random errors. To validate the robustness of our results, we conducted a comparison of constraints derived from different realizations. We aim to assess the extent to which each individual realization biases the constraints. The realizations encompass both white noise and systematic error sources stemming from foreground removal. Within this analysis, we examined the behavior of the five cosmological parameters: Ω_b , Ω_c , h , n_s , and $\ln 10^{10} A_s$, in addition to the 60 nuisance parameters.

The outcomes for three distinct realizations are presented in Figure 2.8. Our observations reveal that the probability contours exhibit some shifts relative to one another across different realizations of the BINGO simulation. This phenomenon can be attributed to the inherent randomness within the simulated data and the degeneracies within the parameter space. Notably, the contours for the same realization but different systematic error sources, i.e., Fig. 2.6, lead to more overlapped contours. However, these shifts are in alignment with the confidence levels associated with the estimated parameter values. Additionally, the contours exhibit similar shapes and sizes across all three scenarios.

2.6.4 BINGO + Planck Λ CDM constraints: Comparison between different realizations

Similar to in the BINGO-only case, we repeated our analysis using the debiased C_ℓ from various realizations of the BINGO simulation. Here, we show the posterior probability contours found from BINGO simulations + Planck 2018 data assuming a flat Λ CDM model. The results for three different realizations are shown in Fig. 2.9. Our observations reveal that the integration of BINGO with Planck 2018 dataset yields increased accuracy on parameter constraining. This combination leads to well-defined parameter values that remain consistent with the Planck 2018 cosmological model. Additionally, we observe that when Planck 2018 data is included, the contours corresponding to different realizations exhibit considerably more overlap than in the BINGO-only scenario.

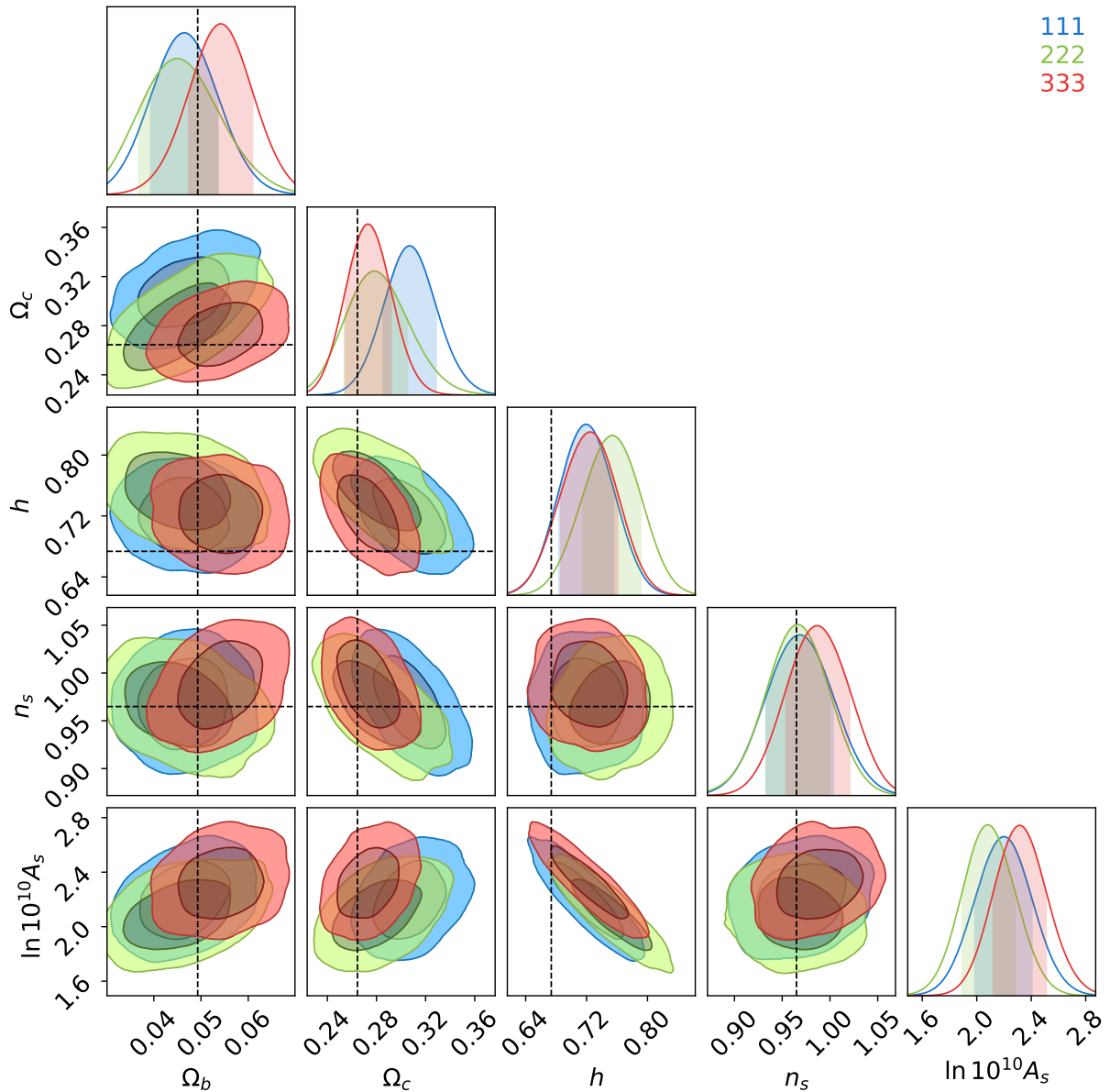


FIGURE 2.8: Λ CDM contours for different realizations of BINGO. The contours were made, including white noise and residuals of foreground removal. It includes the systematic effects of White Nose and foreground removal. Labels 111, 222, and 333 denote the number of realizations in the 500 realizations dataset.

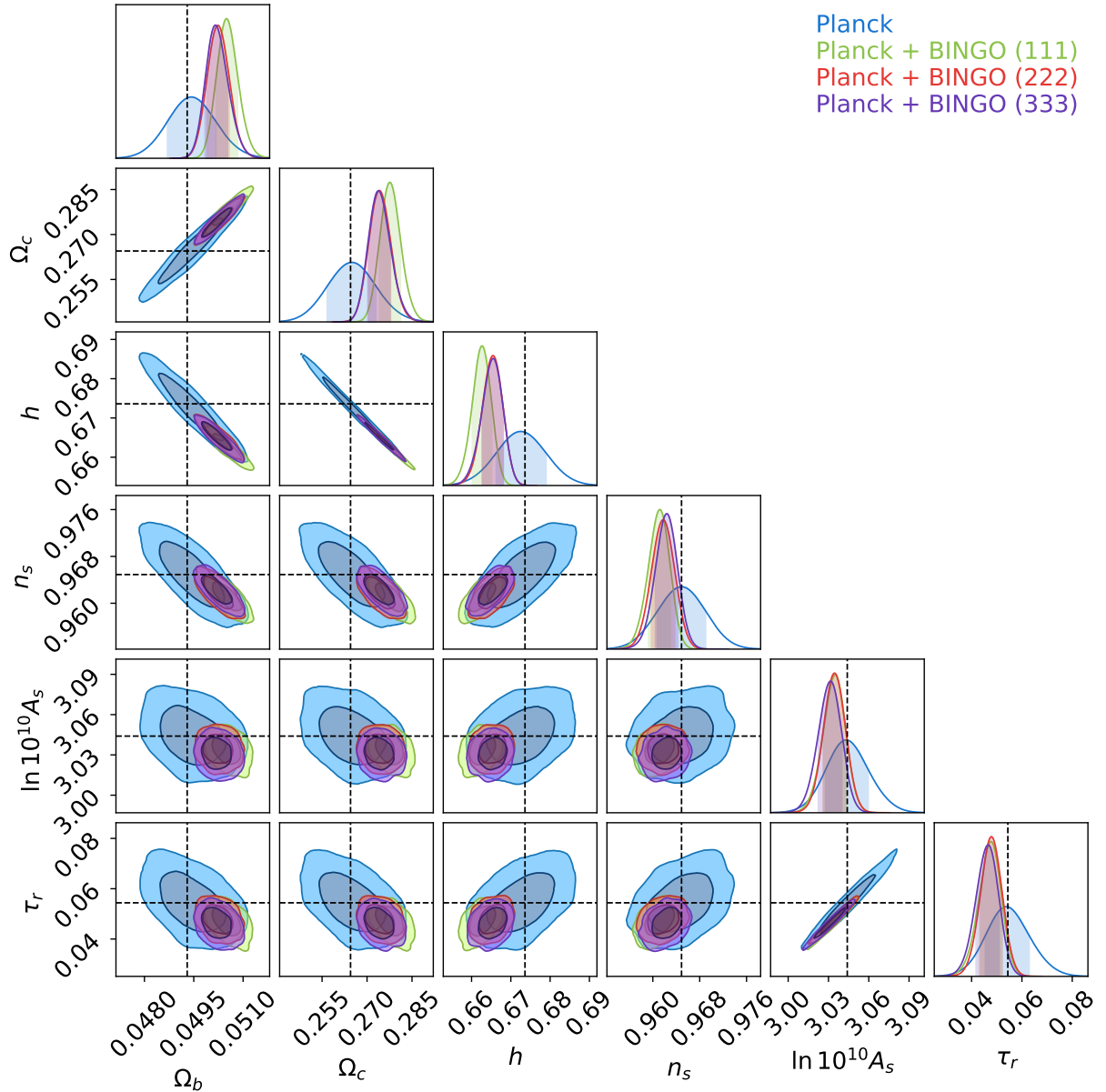


FIGURE 2.9: BINGO + Planck Λ CDM contours for different realizations of BINGO. It includes the systematic effects of White Noise and foreground removal.

2.7 Conclusions

This study investigates cosmological parameter constraints using simulated data from the BINGO experiment, complemented by Planck 2018 data to improve precision. Six key cosmological parameters— Ω_b , Ω_c , h , n_s , $\ln 10^{10} A_s$, and τ_r —and 60 nuisance parameters were analyzed. The study began by assessing the impact of error sources on parameter estimates, starting with the pure 21-cm cosmological signal and extending to include white noise and systematic effects from foreground removal. The results demonstrated that even with systematic errors, the analysis pipeline effectively constrained Λ CDM parameters, maintaining consistent values and confidence levels across different scenarios.

The findings showed strong alignment with Planck 2018 cosmology, except for $\ln 10^{10} A_s$, which was initially degenerate with nuisance parameters $\Omega_{\text{HI}}^i b_{\text{HI}}^i$. Incorporating Planck data resolved this degeneracy, aligning all constrained parameters, including $\ln 10^{10} A_s$, with Planck cosmology within a 2σ confidence level. The combination of BINGO and Planck data significantly improved parameter constraints, even when systematic errors were included. For example, the addition of BINGO data reduced the uncertainty levels for Ω_b , Ω_c , and h by more than 59% compared to Planck-only results.

The robustness of the findings was tested across different realizations of BINGO simulations. Slight variations in probability contours were observed, attributed to random errors in simulated data and parameter space degeneracies. However, the inclusion of Planck data reduced these variations, leading to greater overlap among realizations and highlighting the complementary role of BINGO in cosmological analyses. This study underscores the potential of combining BINGO and Planck data for precision cosmology, even in the presence of systematic uncertainties.

2.8 Next steps

For the final thesis, we will take a closer look at the contours of the nuisance parameters to understand how they contribute to shaping the cosmological parameter constraints. We'll also calculate the χ^2 values for these fittings and compare them across different simulations. This comparison will help us see how white noise and systematic effects impact the accuracy of our parameter estimates. By examining these effects, we can better evaluate the robustness of our analysis pipeline and understand how it performs under different conditions.

Additionally, we know that the fittings can be sensitive to small numerical errors in the computation of the angular power spectrum (APS). Even minor inaccuracies, on the order of a few

percent, can influence the parameter estimation. To address this, we'll look at how controlling numerical precision in the APS calculation can improve our results. We will also consider potential errors introduced by the FLASK map simulation procedure and explore ways to minimize these errors. Finally, we plan to assess how the number of simulations used for constructing the covariance matrix impacts the final χ^2 value and the overall reliability of our parameter constraints. These steps will help us make sure our analysis is as accurate and robust as possible.

Chapter 3

ABDUS project - Implementing outrigger stations with aperture arrays

ABDUS, which stands for *Advanced BAO and Dark Universe Studies*, will be BINGO’s next step toward improving its resolution and coverage. This project is designed to establish BINGO/ABDUS as a leading telescope for detecting Fast Radio Bursts and strong radio point sources (Santos et al., 2024; Zhang et al., 2024). With that aim, BINGO/ABDUS proposes to use detectors in the form of phased arrays, which will allow expressively enlarging the BINGO’s capabilities to reach out to $z \approx 2.1$, for the 21 IM scanning and covering up to 50% of the sky in a resolution between 27'-40', and increasing the current number of beams from 28 up to 200 in a multibeam electronic synthesis through beamformers (Abdalla et al., 2024). This increase will be conducted by joining the already contracted BINGO structure with outrigger and phased array stations.

Despite its primary focus on cosmological investigations, BINGO’s large survey area presents opportunities for supplementary investigations into radio transients. BINGO alone can detect dozens of FRBs annually, with the potential to increase detection rates by approximately 20% with the inclusion of outriggers (Santos et al., 2024). Moreover, employing outriggers can significantly enhance localization capabilities, particularly with two or three baselines, demonstrating the potential for BINGO/ABDUS to contribute to FRB research by enabling the identification of host galaxies and exploring galaxy morphology and formation. Additionally, FRB detection and localization hold promise for refining cosmological parameters.

The BINGO’s today optical configuration is a reflector system with focal-plane arrays (FPAs) (Abdalla et al., 2022c). At a second moment, there will be single-dished outriggers and phased-array stations. The outriggers and phased array stations will be about 20km distant from the main telescope to provide sufficient angular resolution through an interferometric approach to pinpoint FRBs and other possible radio sources (Abdalla et al., 2024). In this chapter, we propose the employment of the Vivaldi antennas (Ruiter et al., 2016) within the BINGO/ABDUS Interferometry System framework.

In this chapter, we present the simulated and measured performance of a 64-element connected Vivaldi antenna array that serves as a prototype tile segment for the envisioned BINGO/ABDUS outrigger stations. This tile prototype is based on the prototypes developed for the mid-frequency aperture arrays envisioned for the Square Kilometer Array Telescope (Ruiter et al., 2016). The tile, therefore, operates in a complementary frequency range to the BINGO main telescope, from 0.5 GHz up to 1.5 GHz, and is capable of producing two independent tile beams per polarization through true-time-delay beamformer integrated circuits (Zhang et al., 2018). An architecture study for the layout of the VAAOS is presented. The beam characteristics of such outrigger stations were simulated with HFSS Ansys (El Mrabet, 2006). The simulations include the VAAOS configurations with 36 and 64 tiles, showing considerable resolution and sidelobe level. The impact of tile spacing on beam patterns is explored. As we still show, our analysis favors dense, connected configurations. Analysis of scan range, effective areas, the impact of beamforming inaccuracies caused by time-delay quantization, and the formation of grating lobes at low elevation angles and high frequencies are detailed.

3.1 Phased array antennas

Phased arrays (PAs) consist of a collection of closely spaced antenna elements, typically separated by approximately half wavelength of the signal they are designed to receive.(Fisher and Bradley, 2000). These arrays have the capability to synthesize multiple independent beams. Among the advantages of phased arrays are precise control over beam patterns, the ability to steer multiple beams, the potential to achieve continuous and uniform sky coverage, an enhancement in the field of view (FOV) through an increased number of beams, resulting in improved survey speed, and broad frequency coverage.

The use of broadband aperture arrays with multibeam techniques has revolutionized astronomical observation by significantly increasing the effective field of view, enabling the observation of large areas of the sky with a wide bandwidth in a short time frame. This advancement is particularly crucial for transient sciences like Fast Radio Bursts (FRBs), with the potential to shed light on the dark energy equation of state. Notable milestones include the Thousand Element Array (THEA; Smolders and Kant, 2000) and subsequent developments such as LOw Frequency ARray (LOFAR; Haarlem et al., 2013), Electronic Multibeam Radio Astronomy Concept (EMBRACE; Kant et al., 2011), and The Murchison Widefield Array (MWA; Lonsdale et al., 2009). These projects have demonstrated the effectiveness of phased-array systems and multibeam beamforming techniques in radio astronomy, paving the way for future cosmological

discoveries and the deployment of advanced instruments like APERTIF (Van Cappellen et al., 2022) with Vivaldi antenna elements.

Phased Array Antennas have the unique ability to change the shape and direction of the radiation pattern without physically moving the antenna. Elements in an antenna array are placed in such a way that the signals transmitted by individual antennas sum up and provide better gain, directivity, and performance in a particular direction. This is achieved by transmitting signals of the same frequency from all the individual elements in the array but with a certain phase difference/shift between each antenna element in the array. In this section, we give an overview of the antenna theory concepts used in this chapter. For a detailed explanation, refer to Balanis, 2016; Mailloux, 2017; Frid, 2020.

3.1.1 Scanning the array

Scanning a phased array involves adjusting the phase of individual elements to steer the main beam toward different angles. This electronic beam steering is achieved without any physical movement of the antenna system. By manipulating the phase relationships between elements, the array can dynamically steer the beam to track targets or efficiently cover specific areas. Introducing a phase shift for each antenna element enables constructive interference in the desired direction while potentially causing destructive interference in other directions. If \mathbf{r}_n is the position of each source of an array it introduces a progressive phase as

$$\psi_n = -k\mathbf{r}_n \cdot \hat{\mathbf{r}}_S \quad (3.1)$$

for each antenna element of the array, enables the array to direct the beam towards the desired scan angle $\hat{\mathbf{r}}_S$.

3.1.2 Array factors

Assuming uniform far-field strength across all radiating elements, the far-field of an array can be predicted based on the far-field of a single element. The array factor, denoted as $AF(\theta, \phi)$, plays a key role in this prediction process. We can express the array field as

$$\mathbf{E}_{array}(\theta, \phi) = AF(\theta, \phi) \mathbf{E}_{element}(\theta, \phi) \quad (3.2)$$

where the array factor $AF(\theta, \phi)$ is defined as

$$AF(\theta, \phi) = \sum_n^N e^{j k \mathbf{r}_n \cdot (\hat{r}(\theta, \phi) - \hat{r}_S)} . \quad (3.3)$$

The summation index n represents the array elements, N is the number of elements, \mathbf{r}_n is the position of each element within the array, and \hat{r}_S is the desired scan direction. That offers a quick method for estimating the far-field of an entire antenna array without the need for exhaustive simulations.

3.1.3 Grating lobes

When the separation between elements in an array is comparable to the wavelength of the radiated waves, interference effects can cause undesired lobes to appear in the radiation pattern, known as grating lobes. To prevent these lobes, a rule of thumb is to ensure that the maximum distance between array elements in a linear scanning array does not exceed a certain limit, as defined by the formula:

$$d = \frac{\lambda}{1 + |\sin \theta_S|} . \quad (3.4)$$

where d is the maximum distance, λ is the wavelength, and θ_S is the scan angle. This guideline helps mitigate the occurrence of grating lobes and ensures a cleaner radiation pattern.

3.2 The technology

Multiple demonstrators and phased array instruments have been constructed within ASTRON, including THEA (Smolders and Kant, 2000), LOFAR (Gunst, Haarlem and Vermeulen, 2011), APERTIF (Van Cappellen et al., 2022), and EMBRACE (Ruiter and Wal, 2009; Kant et al., 2011). As part of the BINGO/ABDUS project, a Vivaldi antenna prototype initially developed for the SKA Mid-Frequency Aperture Array (MFAA) project (Ruiter et al., 2016) at ASTRON is proposed for implementation. A picture of this prototype is shown in Fig. 3.1. It constitutes a dense array comprising dual polarized, connected Vivaldi antenna elements. It offers two independent beams operating within the frequency band spanning 500 to 1500 MHz. The Beamformer chips were developed by Station de Radioastronomie, Nançay (Bosse et al., 2010).



FIGURE 3.1: Prototype tile for the BINGO/ABDUS outrigger station, featuring 64 antenna elements (32 per polarization) arranged in a 0.35 m by 1.34 m array. The elements are angled at 45 degrees relative to the ground plane edges, forming a distinctive W-shaped configuration

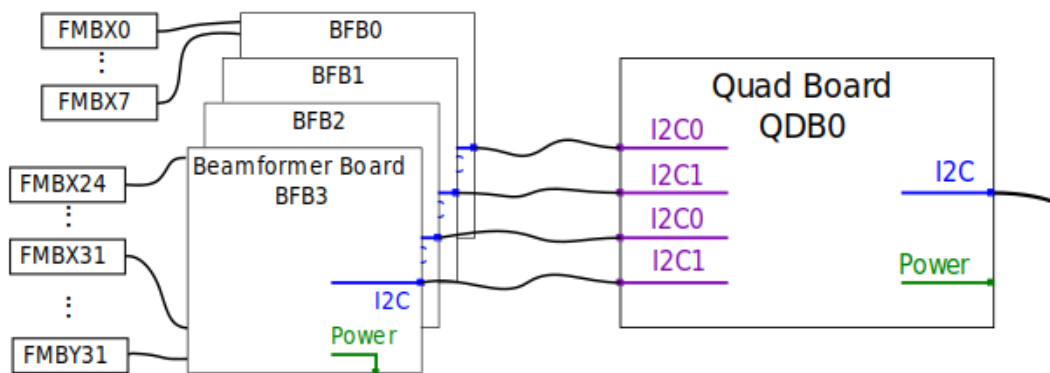


FIGURE 3.2: Schematic of the tile electronics. A Quad Board connects with four Beamformer Boards, which in turn contain four Beamformer chips and are connected to 16 LNAs.



FIGURE 3.3: Positioning of the Low Noise Amplifier (LNA) in the tile design. The LNA is placed next to the square cavity. The tile contains a total of 64 LNAs, one for each antenna element.

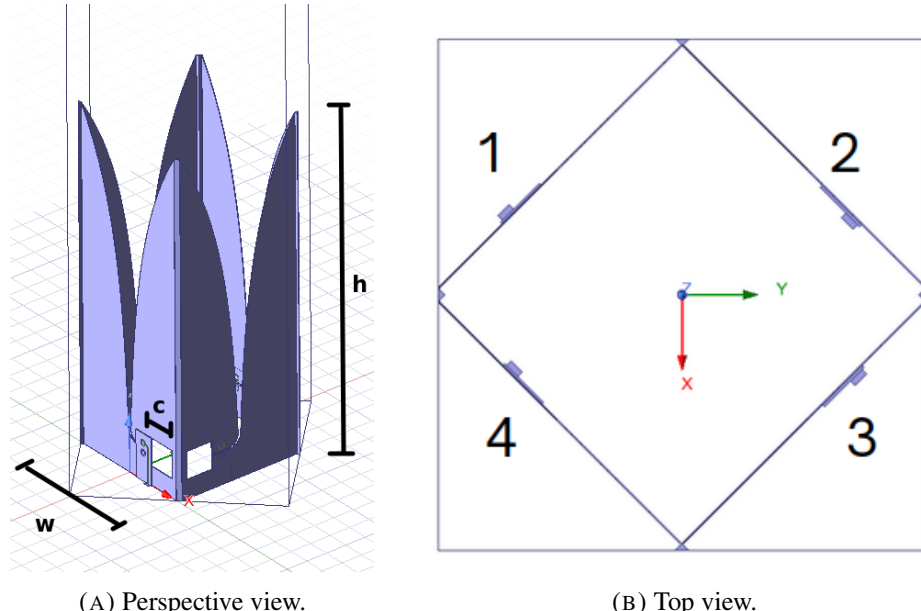


FIGURE 3.4: Perspective and top view of the Vivaldi antenna. Each unit cell has 4 antenna elements. The elements 1,3 are polarized in the same direction, and the elements 2,4 are polarized in the orthogonal direction of them.

3.2.1 Beamforming

The beamforming technique is used to focus the received signal in a specific direction, enhancing sensitivity in a desired direction (Benesty, Chen and Huang, 2008; Mudumbai et al., 2009). A hybrid beamforming concept is applied: the beamforming is achieved in two steps, first in the analog domain to direct the tile beam to the desired scan angle, and then in the digital domain, which reduces the cost of the required digital backend while maintaining beam steering capability (Sohrabi and Yu, 2017; Han et al., 2015; Ioushua and Eldar, 2019; Dutta et al., 2019; Bogale et al., 2016).

The analog beamforming is performed on the small area called a tile (Fig. 3.1), where the output of the Low-Noise Amplifier (LNA) module is connected to the beamformer board for analog beamforming of the tile (Ruiter et al., 2016). Refer to Fig. 3.2 and 3.3 for the schematic of the tile electronics and the positioning of the LNA. The beamformer chips apply true time delay to the RF signal, with each chip capable of beamforming 4 elements and providing two independent beams. By combining beamforming in both analog and digital domains, the phased array system can achieve precise control over the direction of the beam and optimize signal reception based on the application requirements.

3.2.2 True-time delay

True Time Delay (TTD) provides precise control over the phase of each element in the phased array antenna by physically delaying the signal, enabling beamforming in phased arrays (Jung, Yoon and Min, 2020; Singh and Mansour, 2020; Spoof et al., 2020; Deshpande, Heath and Castellanos, 2022; Rotman, Tur and Yaron, 2016; Rahman, 2020). The phase of each element in the array is controlled by delaying the signal by a precise amount of time. TTD differs from Phase Shifters (PS), which directly manipulate the phase of the signals. Phase shifters typically realize a directive array beam in the desired scan direction over a narrow bandwidth: with a constant phase shift applied to all array elements, the array beam squints over a large frequency bandwidth. TTD circumvents beam squint, offering more accurate beam steering across the bandwidth (Chu and Hashemi, 2013; Rotman, Tur and Yaron, 2016).

The TTD implementation for the BINGO/ABDUS Aperture Array involves a beamformer chip design that enables precise control over delay times and channel gains. The chip includes 64 registers assigned to control the delay steps and 16 registers for the channel gains, with two additional registers for controlling extra beam delays after channel combination. This level of control allows for the optimization of beamforming parameters to achieve the desired performance characteristics of the array. Detailed description can be found in Zhang et al., 2018.

3.2.3 Vivaldi Antenna design

A tapered slot antenna is crafted by cutting a slot into a metal surface, where the width of the slot gradually varies (tapers) along its length (Lewis, Fassett and Hunt, 1974). This unique tapering design enables a directional radiation pattern over a broad frequency bandwidth. Tapered slot antennas are also esteemed for their capacity to form wide scanning arrays. One particular variant of these antennas, known as the Vivaldi antenna, features a slot that opens exponentially (Shin and Schaubert, 1999; Gibson, 1979). The slot profile of this specific radiator is mathematically described as $x = a + be^{rz}$, with $a = 2.491$ mm, $b = 3.941$ mm, and $r = 0.01$ mm $^{-1}$. Refer to Fig. 3.4a for a scheme if this design. The antenna itself boasts a width (w) of 118 mm, a height (h) of 316 mm, a thickness of 0.5 mm, and extends 26 mm on each side (c) of the square cavity. The antenna elements are arranged at a 45-degree angle with respect to the ground-plane edges, forming a distinctive W-shaped array configuration. This configuration comprises four labeled antenna elements: 01, 02, 03, and 04, where elements 01 and 03 (Fig. 3.4b) share the same polarization, while elements 02 and 04 share a similar polarization, orthogonal to that of 01 and 02. The tile prototype incorporates a total of 64 antenna elements, evenly distributed between polarizations, arranged in a planar array measuring 0.35m x 1.34m.

3.3 Science requirements

The main focus of BINGO/ABDUS is to study dark energy using neutral Hydrogen emission lines (Abdalla et al., 2022a). Additionally, BINGO/ABDUS can detect and pinpoint Fast Radio Bursts (FRBs) through an interferometry system, which includes smaller auxiliary radio telescopes known as outriggers. Interferometry involves multiple telescopes observing the same sky region simultaneously, correlating signals to measure time delays between the arrivals at different telescopes. For the cross-correlation of telescopes, the minimum flux density is given by

$$S_{min}^{intf} = \frac{1}{\sqrt{2n_p \Delta\nu \tau}} \left\{ \sum_{ij} \frac{G_i P_{n,i}(\mathbf{n})}{K_i T_{sys,i}} \frac{G_j P_{n,j}(\mathbf{n})}{K_j T_{sys,j}} \right\}^{-\frac{1}{2}} \quad (3.5)$$

where the indexes i, j denote the distinct telescopes of the system, T_{sys} is the system temperature, G is the forward gain, $P_n(\mathbf{n})$ is the antenna pattern normalized to one at the peak, $K = \sqrt{2}$ for a correlation receiver, n_p is the number of polarizations, $\Delta\nu$ is the bandwidth, τ is the sampling time (Walker, 1999). The scientific requirements for such systems include therefore high time resolution to capture the brief bursts, precise synchronization of telescopes to

accurately measure time delays, a wide field of view to increase detection chances, low system temperature and advanced data processing capabilities to handle the large volumes of data and perform real-time signal correlation and localization of the FRBs.

The BINGO IX paper (Santos et al., 2024) investigated FRB detection capabilities for the BINGO/ABDUS Interferometry System (BIS). BIS combines the BINGO radio telescope with auxiliary outriggers to localize fast radio bursts (FRBs) in the sky. BIS is capable of detecting dozens of FRBs using 5 to 10 single-dish outriggers with mirrors ranging from 4 to 6 meters in diameter.

In this paper, we propose the integration of a Vivaldi Aperture Array Outrigger Station (VAAOS) within the BINGO/ABDUS interferometry system framework. To enable effective interferometry, the VAAOS optical Field of View (FoV) must cover BINGO's instantaneous focal plane area, which measures 14.75 x 6 degrees. To achieve a low minimal flux density for detecting weak Fast Radio Bursts (FRBs), the sensitivity of the VAAOS is a crucial factor. A larger effective area enhances sensitivity, allowing for the detection of lower flux densities. In this context, we propose outrigger stations with effective areas of 10 to 30 square meters. These stations would improve the overall sensitivity of the BINGO/ABDUS system, ensuring it can detect the faintest FRB signals. Refer to Santos et al., 2023 for detailed discussions on the effective area requirements.

3.4 Simulated results

For our simulations, we used Ansys HFSS (High-Frequency Structure Simulator) (El Mrabet, 2006) a commercial software that solves electromagnetic (EM) problems using the finite element method.

In our HFSS setup, we only excite sources 01 and 03 with 1W, while sources 02 and 04 remain passive (0W). When scanning the zenith, the input phases are set as follows: 0° for sources 01 and 02, and 180° for sources 03 and 04 because the mirrored LNA's result in oppositely polarised fields at the antenna aperture.

The tile geometry is modeled in HFSS as a regular array consisting of 16 unit cells, arranged in two columns of eight cells each. Each unit cell contains four antenna elements, as described in Sec. 3.2.3. This configuration is illustrated in Fig. 3.5. To create the array structure, we applied the HFSS master/slave boundary condition, which defines primary and secondary boundaries to ensure periodicity and proper field behavior across the array. The results are shown as function of the θ, ϕ spherical coordinates, defined with respect to the Cartesian frame illustrated in Fig. 3.5a.

3.4.1 Tile simulation

In this section, we present the electromagnetic simulations for the tile prototype. We begin by comparing the simulated pattern, which accounts for mutual coupling effects between array elements, with the ideal pattern, which does not. The far-field of the tile, computed using Array Factors, is shown by the yellow curve in Fig. 3.6, while the full HFSS simulation, incorporating coupling effects, is represented by the green curve.

The Array Factors method provides an approximate solution, as it neglects mutual coupling, leading to slight deviations from the full simulation results. Despite this, the comparison shows that the ideal pattern aligns closely with the full HFSS simulation, indicating that mutual coupling has a relatively modest impact on the overall beam shape. Both patterns exhibit similar trends, with the primary difference being slightly higher values in the HFSS simulation for angles closer to the horizon. However, this difference remains minimal in the main lobe and first sidelobes, suggesting that while coupling exists, it does not significantly degrade the tile's performance in terms of beam characteristics.

The tile's beam exhibits a gain of 5.02, dBi, with a full-width at half-maximum (FWHM) of 42° along the x -axis and 10° along the y -axis. The x and y -axis correspond the minor and major axis of the tile, as shown in Fig. 3.5a. A 3D representation of the beam pattern is shown in Fig. 3.5b. The narrower FWHM along the y -axis is due to the higher number of antenna elements arranged in this direction, which results in a more focused beam. This arrangement also explains the presence of sidelobes observed exclusively along the y -axis, with the first sidelobe being -13.3 , dB relative to the main lobe. Furthermore, this size comfortably envelops the area of the BINGO main telescope, ensuring full coverage of its field of view and enabling effective interferometry.

Polarization

The electromagnetic simulation of the tile also provides insights into the polarization components, particularly the cross-polarization levels. Fig. 3.7a illustrates the cross-polarization performance of the tile prototype. The analysis shows that the tile exhibits a favorable cross-polarization level, with a significant difference between co-polarization and cross-polarization, especially at the main lobe. Specifically, the cross-polarization is 26.4 dB lower than the co-polarization at the main lobe, indicating a good polarization purity. As we move towards the horizon, the difference between the co-polarization and cross-polarization decreases, but overall, the tile maintains strong polarization isolation, particularly in the region of interest around

the main lobe. This characteristic ensures that the tile will perform well in applications requiring minimal cross-polarization interference. The Stokes parameters are shown in Fig. 3.7b. This simulation helps verify that the beam is nearly unpolarized, while still accounting for slight imbalances between polarization states.

Effect of delay quantization

The True-Time Delay in the beamformer chip adjusts the time delay of signals in discrete steps. These delay steps determine the resolution with which the chip can steer the beam. The smaller the delay steps, the finer the control over the direction of the beam. Each time delay step is related to a frequency-dependent phase shift; for instance, the implemented beamformer chip has a delay step of 20 ps, which results in a 7.2° phase shift at 1 GHz and a 10.8° phase shift at 1.5 GHz. In this section, we examine the impact of different levels of delay quantization on the beamforming resolution.

The effect of time-delay quantization for the implemented beamformer chip is illustrated in Fig. 3.8. The blue curve represents the beam pattern at 1 GHz without phase quantization, scanned at an angle of $\theta = 20^\circ$, $\phi = 90^\circ$. The orange curve shows the beam pattern with delay quantization, assuming a delay step of 20 ps. We observe notable discrepancies in the sidelobes, with minimal differences at the main lobe. Fig. 3.9 displays the errors due to delay quantization, calculated as the dB difference between the beam patterns with and without delay quantization, and compares different time-delay steps at frequencies of 1 GHz and 1.5 GHz.

As expected, phase quantization introduces minor deviations from the ideal beam pattern, with errors becoming more significant as the delay step increases. Additionally, at higher frequencies, each time-delay step translates to a larger phase step, amplifying the quantization effect. This results in more pronounced discrepancies in the sidelobes and at local minima. For smaller delay steps, such as 20ps and 10ps, the differences remain relatively minor, showing that the beam pattern approximates the ideal case well. With a 20ps delay step, the average difference is 0.45dB at 1GHz and 1dB at 1.5GHz. This analysis indicates that the deployed technology, with a 20ps delay step, enables beamforming with precise resolution, though the effect of quantization becomes more pronounced at higher frequencies.

3.4.2 Outrigger station simulations

In this section, we present the results for two simulated outrigger stations. The first station is composed of 36 tiles arranged in an approximately rectangular configuration measuring 4.22m by 4.02m. The second station consists of 64 tiles, with a larger rectangular layout measuring

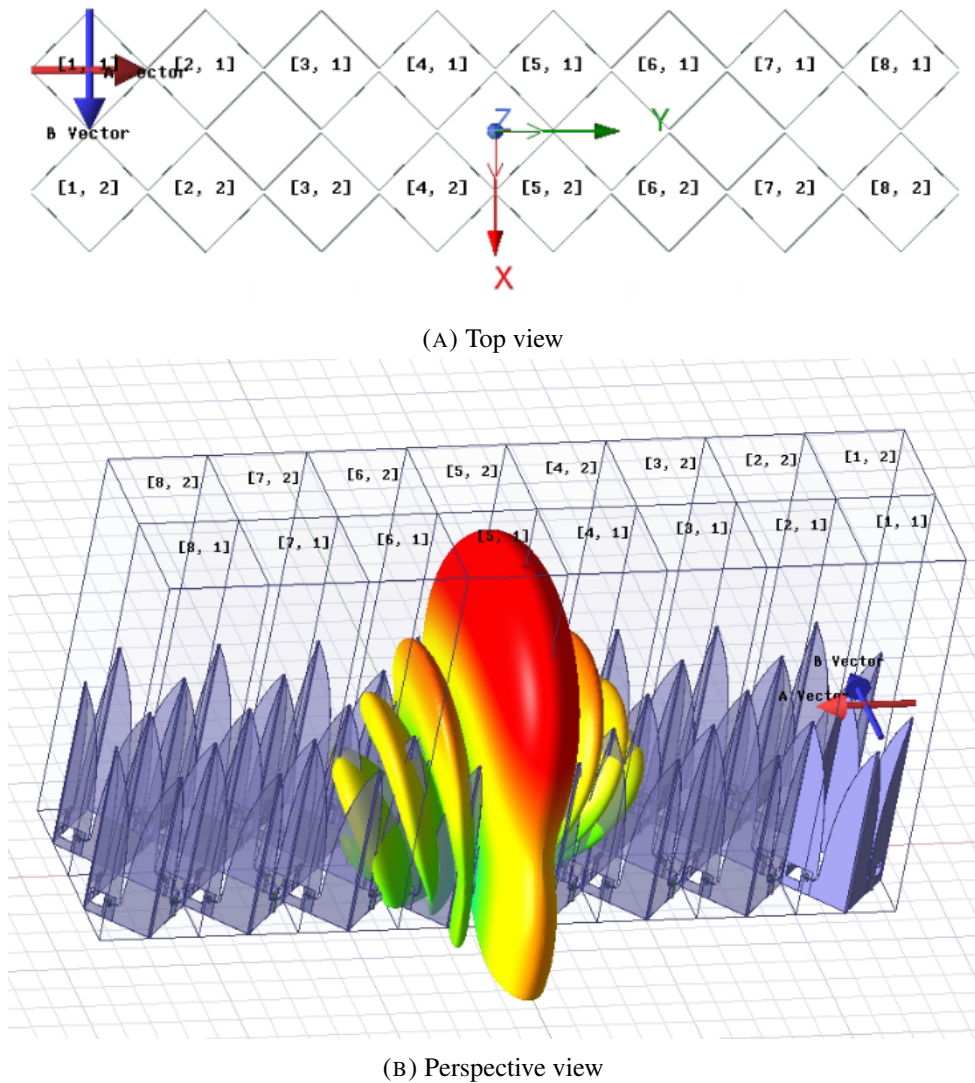


FIGURE 3.5: Top: Top view of the tile within HFSS software. The coordinate system is defined such that the x and y axes are aligned with the minor and major axes of the tile respectively. Bottom: perspective view of the tile within the HFSS software. The simulated 3D beam pattern is projected on top of the tile. Sidelobes are formed along y -axis. The FWHM in x and y directions are 42° and 10° , respectively.

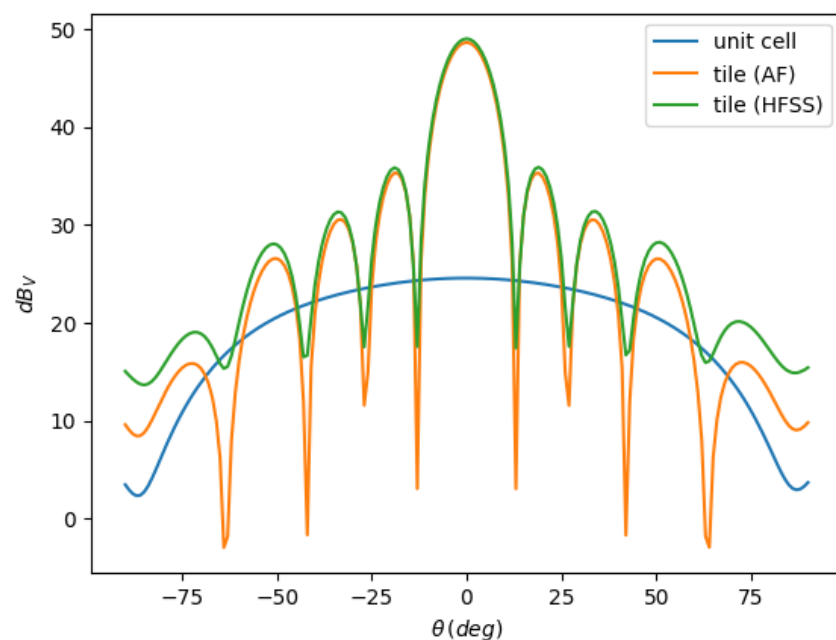
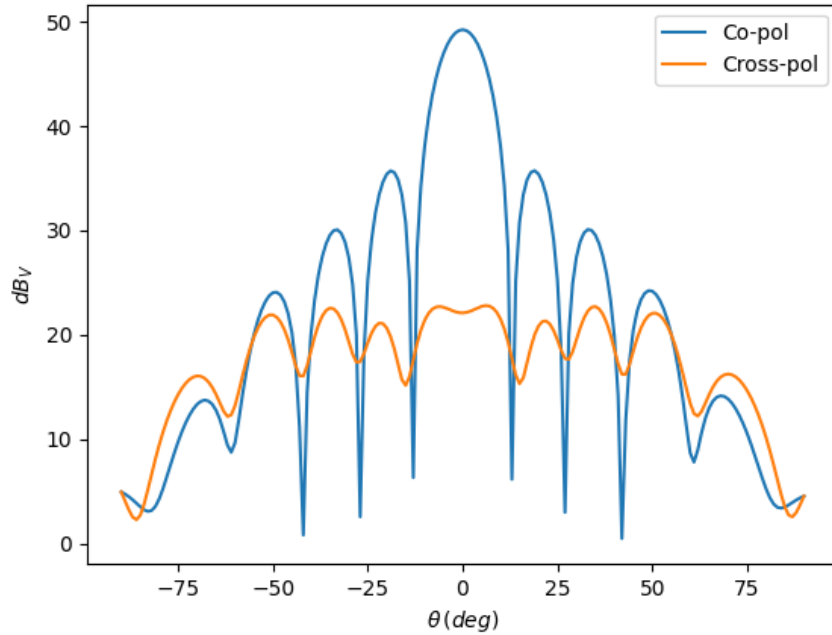
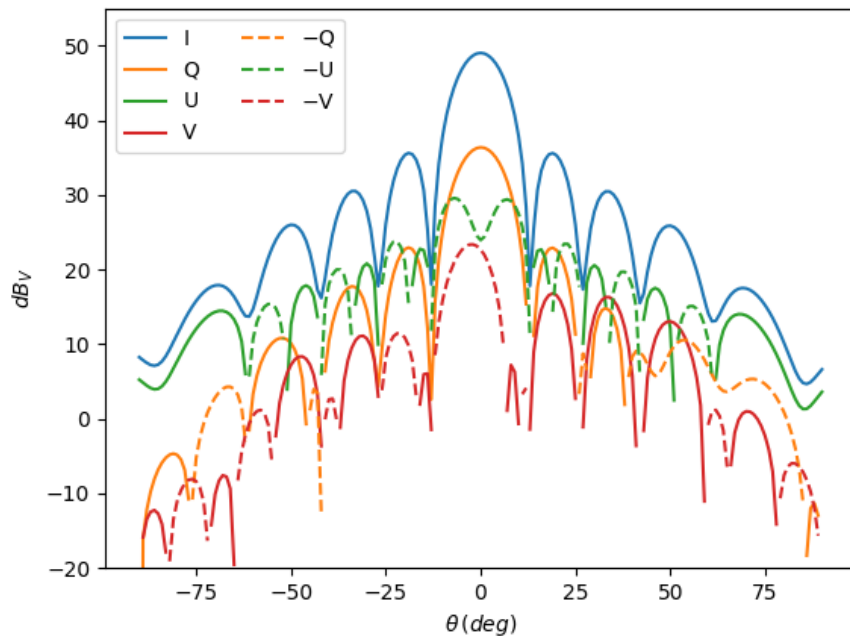


FIGURE 3.6: Beam pattern of the tile at 1GHz. We compare the field of a unit cell (blue) with field of the tile simulated with HFSS (green) and the one computed using array factors (yellow). The HFSS simulated field takes into account the mutual coupling between the antenna elements.



(A) Polarization components.



(B) Stokes parameters.

FIGURE 3.7: Top: co-polarization and cross-polarization of the tile. The difference between the co and cross-polarization is 26.4dB at the main lobe. Bottom: Stokes parameters for an unpolarized beam, computed by averaging the Stokes parameters of two orthogonal linearly polarized beams. The solid lines are the positive parameters and the dashed lines are the negative parameters. The Stokes parameters I, Q, U, V have maximum values of 49dB, 36.4dB, 29.6dB and 23.4dB.

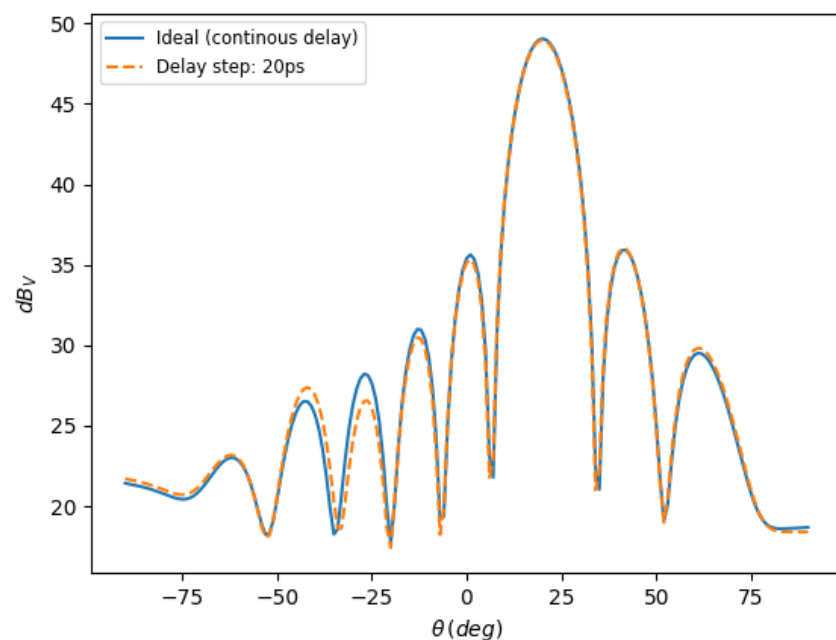
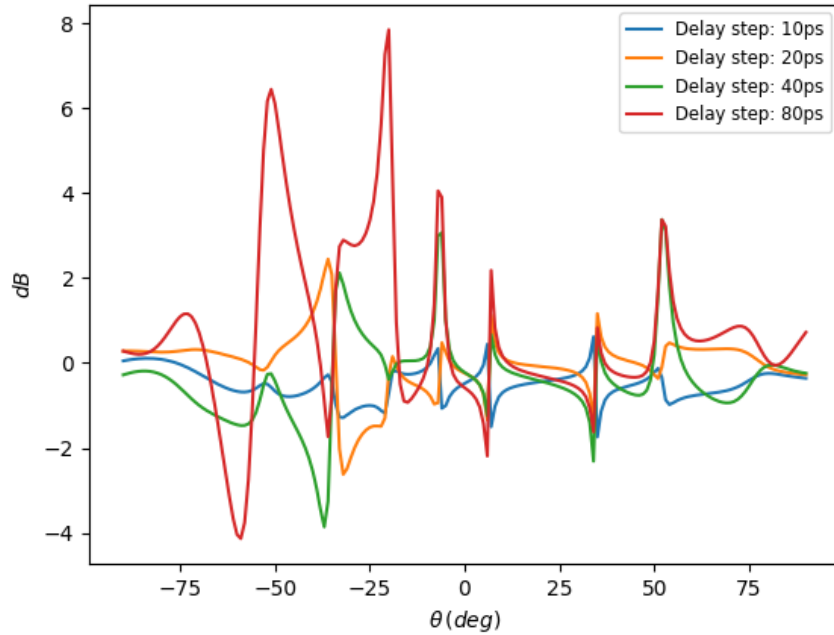
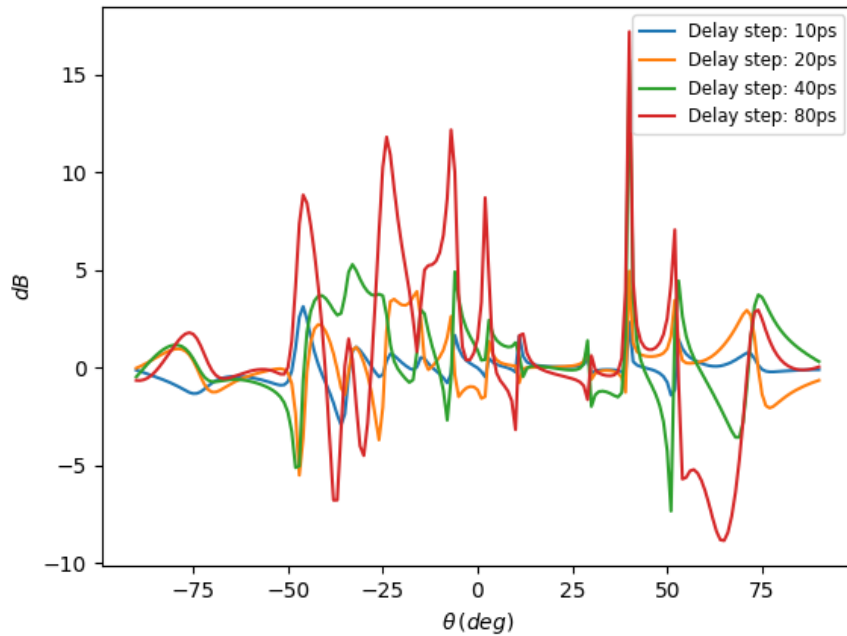


FIGURE 3.8: Beam pattern comparison at 1GHz with and without time-delay quantization. The blue curve represents the tile beam pattern at 1 GHz, scanned at angles $\theta = 20^\circ$, $\phi = 90^\circ$, with no time-delay quantization applied. The orange curve shows the beam pattern under a 20ps time-delay quantization step.



(A) Error of time-delay quantization at 1GHz



(B) Error of time-delay quantization at 1.5GHz

FIGURE 3.9: Left: Difference in dB between the beam pattern with time-delay quantization and without, at 1 GHz. This difference is shown for various time-delay steps: 10ps, 20ps, 40ps, and 80ps. Right: The same comparison at 1.5GHz. At higher frequencies, each time-delay step translates to a larger phase step, amplifying the quantization effect. Quantization primarily impacts the sidelobes, with minimal effect on the main lobe

5.63m by 5.36m. These stations are organized with side lengths of 3 and 4 tiles respectively, arranged longitudinally. Refer to Fig. 3.10a.

For both stations, the beam pattern is analyzed. The pattern for the frequency of 1GHz is shown in Fig. 3.10b. Some data are summarized in the Table 3.1. The full width at half maximum (FWHM) is 4 degrees for the 36-tile station and 2 degrees for the 64-tile station, indicating a sharper focus of the signal. The 64-tile station demonstrates a gain nearly seven times greater as the one of the single tile. The beam pattern also exhibits well-controlled sidelobes, with the first sidelobe being approximately $-13dB$ below the main lobe, as illustrated in the figures.

Stations with randomly spaced tiles

The stations simulated earlier were modeled as dense arrays with no spacing between tiles. However, spacing between the tiles can be treated as a free parameter that may be adjusted to mitigate sidelobes. Care must be taken when spacing the tiles, as improper spacing can lead to the formation of grating lobes, which can degrade the overall beam quality.

Initially, a uniform spacing of 10cm (5cm) was applied in both the horizontal and vertical axes. Our findings show that the regular 10 cm spacing indeed leads to the formation of grating lobes. In the 36-tile array, 12 tiles are disposed crosswise in the $\phi = 0^\circ$ plane, and three tiles are disposed longitudinally in the $\phi = 90^\circ$ plane. The grating lobes are most prominent in the $\phi = 0^\circ$ plane, in which the total space added is larger.

Attempting to mitigate the formation of grating lobes, we introduced random spacing between the tiles. A random offset was added to the uniform space, drawn from a uniform distribution between -5cm and 5cm (-2.5cm and 2.5cm). These results are portrayed in Fig. 3.11. When random spacing was applied, the beam patterns remained very similar to those with regular spacing, with only minimal mitigation of the grating lobes and no notable reduction in sidelobe power.

Furthermore, as the spacing between tiles was decreased, the grating lobes also diminished. However, even with randomization, the grating lobes did not disappear, and the sidelobe levels remained unchanged. Thus, our analysis suggests that the best configuration remains the dense array with no spacing between the tiles. Despite the introduction of randomization, grating lobes persist with increased tile spacing, and their mitigation is not easily achieved through these methods.

Scan angle and effective area

In HFSS, we simulated a scanned beam by introducing a progressive phase shift. The beam patterns for different scan angles of the 36-tile station are shown in Fig. 3.12a, with the scanned patterns represented by solid lines. Our findings indicate that the peak of the main lobe decreases as the scan angle increases. This reduction occurs because, although the Vivaldi unit-cell field is broad (as shown by the blue curve in Fig. 3.6), it diminishes at higher θ angles, which influences the field of the array.

To further analyze the performance, we calculated the effective area of the outrigger station for various frequencies and scan angles using the equation:

$$A_{eff}(\theta, \phi) = \frac{\lambda^2}{4\pi} G(\theta, \phi), \quad (3.6)$$

where G represents the gain at the peak of the main lobe (Rohlfs and Wilson, 2013). Fig. 3.12b displays the effective area as a function of the scan angle for frequencies of 0.5 GHz, 1 GHz, and 1.5 GHz. In the same figure, the effective area is compared to the physical area, which is modulated by $\cos \theta_S$.

For example, at 1 GHz and a scan angle of $\theta_{scan} = 40^\circ$, the physical area is reduced to 78% of the area at zenith. In general, scanning is most efficient when the scan angle θ_{scan} is less than 45° , as scanning beyond this limit results in significant losses in both gain and effective area. Additionally, grating lobes negatively affect the effective area, particularly at higher frequencies. When grating lobes form at large scan angles, they draw power away from the main lobe, reducing its gain and the station's effective area.

This explains why, for the same scan angle, the effective area decreases more significantly at higher frequencies. A more detailed discussion of the impact of grating lobes will be covered in the next section.

Scan angle and grating lobes

Grating lobes tend to appear at high frequencies and large scan angles, leading to multiple maxima in the radiation pattern of the array. For example, as seen in Fig. 3.12a, the red line corresponding to a scan angle of $\theta = 60^\circ$ shows a main lobe at $\theta \approx 60^\circ$ and a grating lobe at approximately $\theta \approx -70^\circ$.

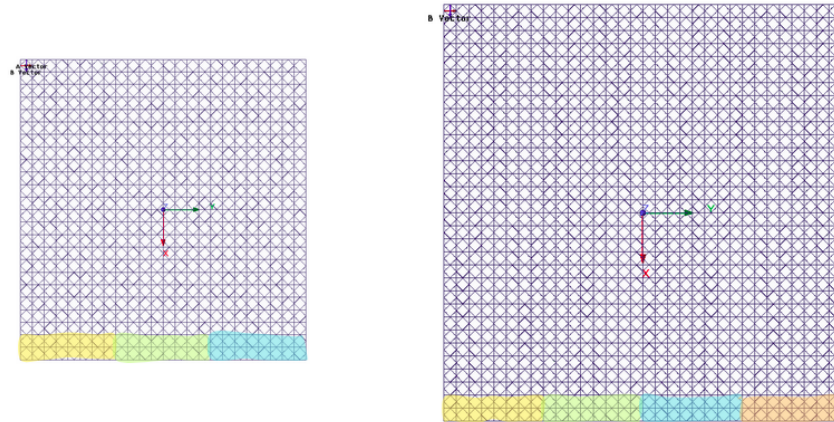
To better understand the behavior of grating lobes for VAOOS, we computed the field of the scanned station using both HFSS simulations and array factors. As shown by Fig. 3.12a, the

	01 tile	36 tiles	64 tiles
Size (m x m)	0.35 x 1.34	4.22 x 4.02	5.63 x 5.36
Gain (dBi)	5.02	33.6	36.1
Phis. area (m ²)	0.47	17	30.2
Eff. area (m ²)	0.45	16.2	28.8
FWHM (deg)	10 (42)	4	2
First side lobe (deg)	-13.3	-13.3	-13.9

TABLE 3.1: Technical data for the tile and for the 36-tile and 64-tile station. All the quantities except the size and physical area were computed from the HFSS simulations.

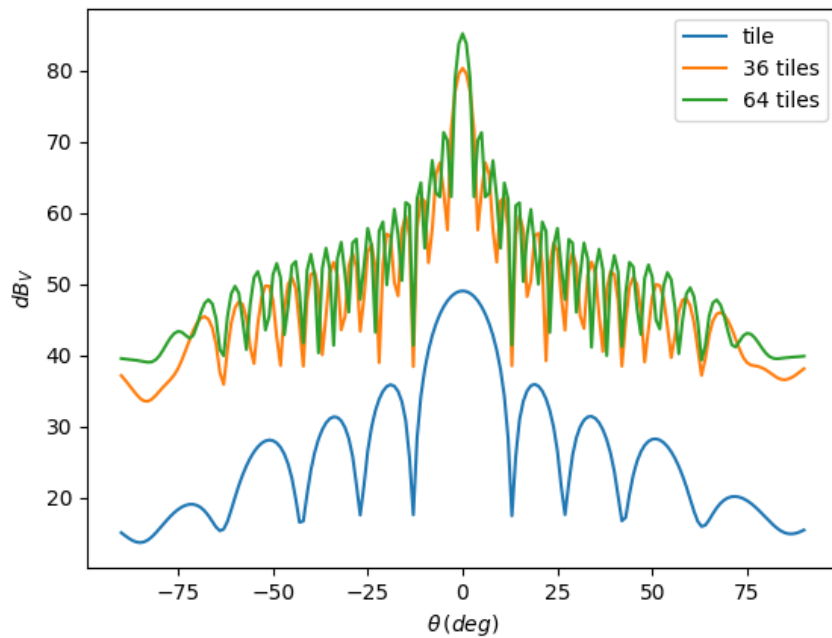
array-factor predictions align closely with the full simulation results for small scan angles. Despite small discrepancies, array factors can still be used as a reliable approximation to determine the maximum scan angle before grating lobes become problematic.

To prevent grating lobes from interfering with the main beam, we calculated the maximum scan angle as a function of frequency in which we can steer the beam such that grating lobes are not formed. This result is shown in Fig. 3.13, where we explore grating lobes for multiple frequencies and scan angles. In this analysis, the calculation was done with Array Factors, instead of full array simulation. We scan $\theta_{\text{scan}} > 0$ and the grating lobes are formed at $\theta_{\text{scan}} < 0$. The function shown in Fig. 3.13d is the difference between the main lobe and the largest value at $\theta_{\text{scan}} < 0$, which is equal to the difference between the main lobe and the largest grating lobe when a grating lobe is formed. This function is decrescent for large θ_{scan} indicating a grating lobe that increases with the scan angle. However, for some frequencies it also has a saddle point before becoming a decrescent function. The saddle points are related to the formation of lobes at $\theta = -90^\circ$, while the decrescent part of the function is due to the grating lobes formed at $-90^\circ < \theta < 0^\circ$. The maximum scan angle (θ_{max}) is defined such that the function depicted in Fig. 3.13d is lower than a given threshold. We computed θ_{max} for the thresholds of 10dB, 14dB and 15dB. The θ_{max} as function of frequency is shown in Fig. 3.13e. At higher frequencies, the grating lobe effect becomes more pronounced. For example, for a frequency of 0.9 MHz, the maximum scan angle without significant grating lobes is approximately 70° , but this angle decreases to around 10° at 1.5 GHz. Our analysis shows that for frequencies below 1 GHz, we can safely scan up to 45° without encountering grating lobes.



- 24x24 unit cells
 - 36 tiles
 - 422cm x 402cm
 - Physical area: 17m²
 - Effective area: 16.24m²
- 32x32 unit cells
 - 64 tiles
 - 563cm x 536cm
 - Physical area: 30.21m²
 - Effective area: 28.84m²

(A) Top view of outrigger stations



(B) Beam pattern of stations

FIGURE 3.10: On top we see the topview comparison between the 36-tile station and the 64-tile station. They have respectively a side length of 03 and 04 tiles. The beam pattern of both configurations are portrayed on the bottom together with the beam of a single tile.

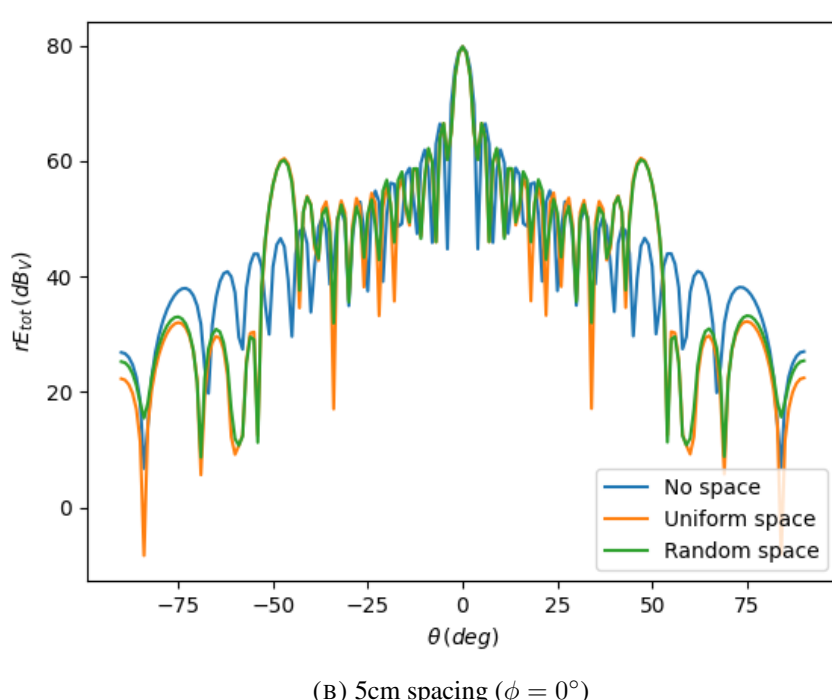
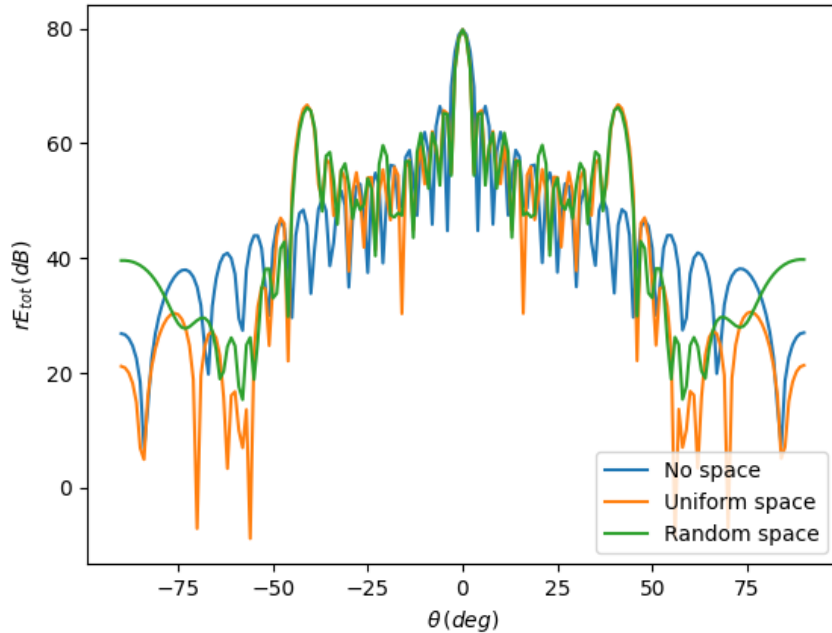
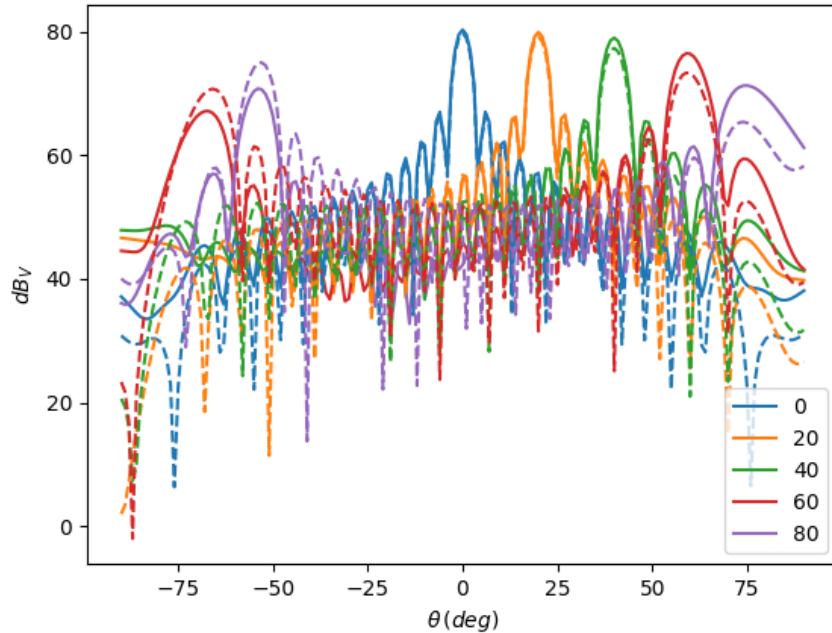
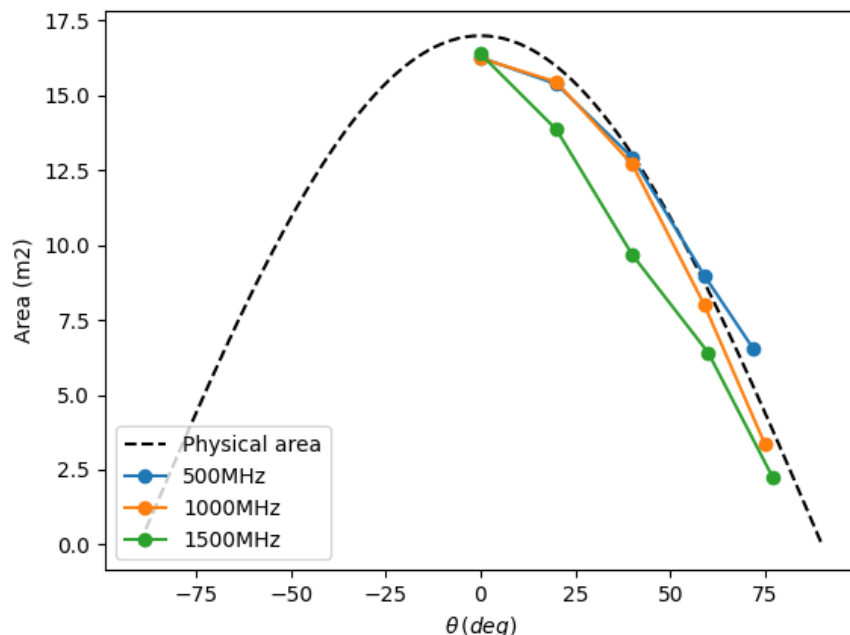


FIGURE 3.11: The blue line is the standard beam pattern of the station of 36 tiles without any spacing between the individual tiles. In Fig. 3.11a (Fig. 3.11b), the yellow line is the corresponding pattern when a space of 10cm (5cm) is introduced between the tiles. The green line is pattern when the position of each tile is uniformly randomized in $\pm 5\text{cm}$ ($\pm 2.5\text{cm}$) with respect to the spaced position. We find that spacing the tiles create undesired grating lobes. The randomization attenuates but not solve this issue. This analysis favors non-spaced stations.



(A) Beam pattern for different scan angles



(B) Effective area

FIGURE 3.12: Top: Beam pattern of the 36-tile station at 1GHz for different scan angles. The solid lines are the HFSS simulated field for different scan angles, i.e: 0°, 20°, 40°, 60° and 80°. The dashed lines are the same patterns but computed with array factors. Bottom: Effective area as function of the scan angle for different frequencies. The blue, orange and green line are respectively frequencies of 500MHz, 1000MHz and 1500MHz. The black solid line is the physical area multiplied by the cosine of the scan angle.

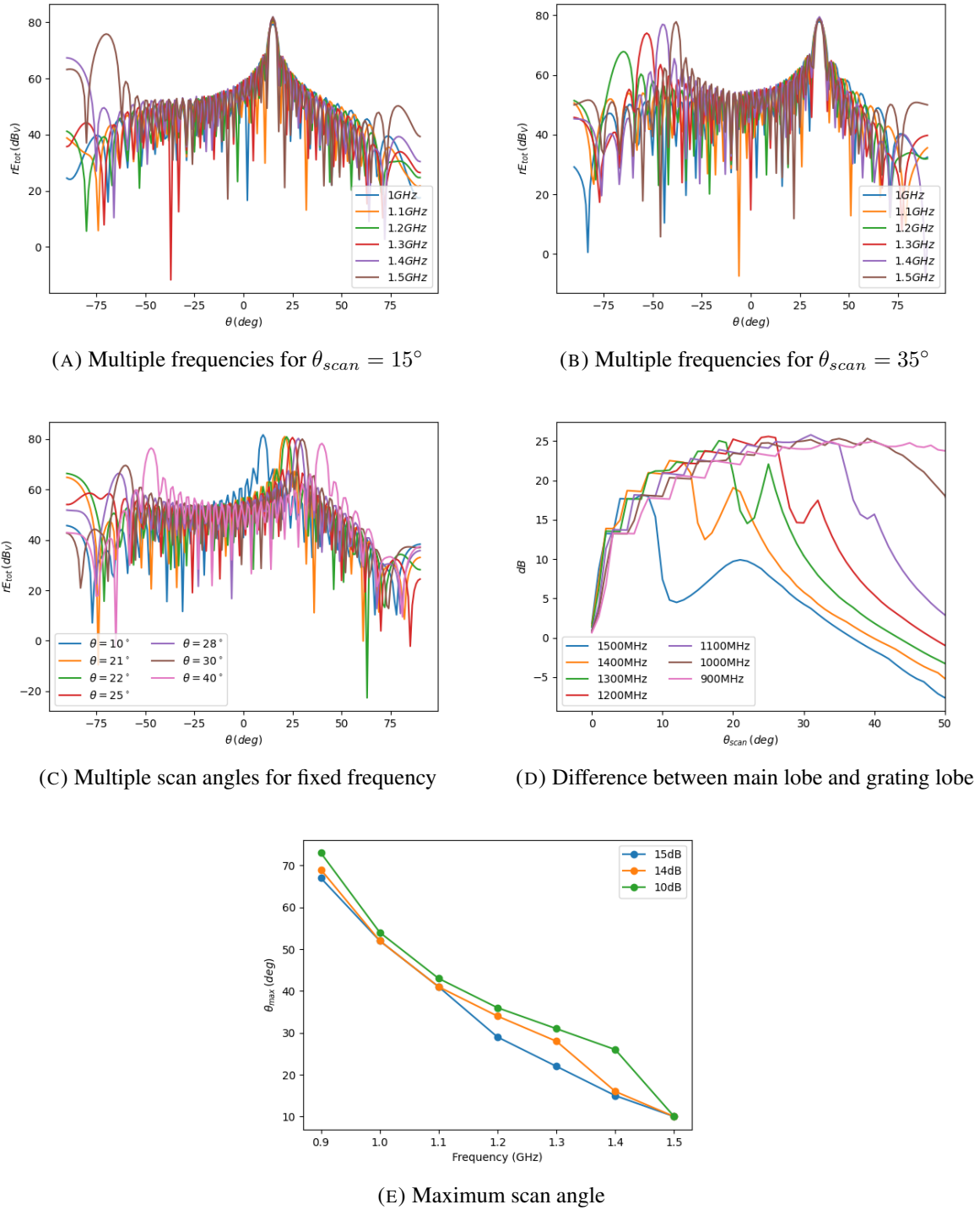


FIGURE 3.13: We explore the formation of grating lobes over the scan angle for different frequencies. Then, we computed the maximum scan angle in which the difference between the main lobe and the grating lobe is lower than a threshold of 10, 14 and 15dB respectively. The maximum scan angle is $\approx 70^\circ$ for 0.9MHz and decreases to $\approx 10^\circ$ for 1.5MHz.

3.5 Conclusions

The analysis and simulations presented offer a comprehensive understanding of the performance and design considerations for the tile prototype and outrigger stations intended for use in the BINGO/ABDUS interferometry system. Array factor predictions, though approximate due to the neglect of mutual coupling, closely aligned with full HFSS simulations, providing efficient far-field estimations. Our investigations revealed crucial insights, including that the single tile prototype, featuring 64 antenna elements, exhibits a gain of 5.02 dBi with a full-width at half-maximum (FWHM) of 42° along the x-axis and 10° along the y-axis. This configuration ensures that the tile comfortably envelops the area of the BINGO main telescope, enabling effective interferometry. Our evaluations highlight the impact of grating lobes at increased frequencies and angles, with maximum scan angles to avoid grating lobes decreasing at higher frequencies.

We demonstrated that outrigger stations comprising 36 and 64 tiles can achieve effective areas of 17m² and 30.2m², respectively, which are sufficient for the detection of hundreds of Fast Radio Bursts (FRBs) annually (Abdalla et al., [n.d.](#)). The analysis also indicates a favorable cross-polarization level, with a significant difference of 26.4 dB between co-polarization and cross-polarization at the main lobe, suggesting good polarization purity essential for minimizing cross-polarization interference in applications. Additionally, we found that phase quantization introduces minor deviations from the ideal beam pattern, with smaller delay steps, such as 20ps and 10ps, maintaining a beam pattern closely approximating the ideal case.

Chapter 4

Final remarks

In conclusion, this work presents significant advancements in both the observational and technical capabilities of the BINGO experiment, underscoring its potential as a valuable tool in cosmology and radio astronomy. Through a detailed analysis of cosmological parameter constraints, we showed that BINGO, particularly when combined with Planck 2018 data, can provide robust constraints on Λ CDM parameters, effectively enhancing the precision of late-time cosmological measurements. Our work demonstrates our pipeline ability to handle systematic and random errors, offering reliable parameter estimates. This establishes BINGO as a promising instrument for future HI intensity mapping, contributing meaningful insights into the large-scale structure of the Universe. In future projects, this analysis can be extended to explore cosmological models beyond Λ CDM, including dark energy-dark matter interaction models and modified gravity theories.

On the technical side, the design and performance evaluation of the Vivaldi tile prototype and outrigger stations have laid a strong foundation for BINGO/ABDUS's interferometric system. Our results confirmed that the tile configuration meets gain and beamwidth requirements, ensuring broad coverage for the main telescope's field of view and promising effective detection of Fast Radio Bursts (FRBs). The analysis highlighted critical design considerations, such as polarization purity and grating lobe management. Upcoming system temperature measurements and calibrated beam pattern assessments will enable a more realistic evaluation of the system's sensitivity. Our initial study of the outrigger station architecture indicated a preference for a dense configuration. However, in future projects, we plan to investigate non-dense configurations that could reduce sidelobe contamination while enhancing overall sensitivity and precision.

Overall, this thesis shows that BINGO/ABDUS's are well-suited to contribute significantly to 21-cm cosmology and radio transient detection. BINGO/ABDUS not only offers a means to achieve more precise constraints on cosmological parameters but also serves as a valuable platform for advancements in radio interferometry, paving the way for its future role in expanding

our understanding of the Universe.

Beyond these contributions, BINGO/ABDUS's role in 21-cm cosmology can be further strengthened through cross-correlation of BINGO's intensity mapping with optical survey data, potentially improving cosmological parameter constraints. In this context, I am also involved in a complementary project using data from optical surveys, particularly SDSS spectroscopy and DES photometric data. This project focuses on object classification to mitigate contamination from local sources and on photometric redshift estimation with machine learning techniques. This analysis will be included as a chapter in the final PhD thesis.

My PhD research is expected to culminate in three first-author papers: Chapter 2 and Chapter 3 correspond to two of these papers, both currently undergoing internal review within the BINGO collaboration. The third one will be derived from my work on the optical data project.

Bibliography

- Abbott, TMC et al. (2019). ‘Dark energy survey year 1 results: constraints on extended cosmological models from galaxy clustering and weak lensing’. In: *Physical Review D* 99.12, p. 123505.
- Abdalla, Elcio et al. (2022a). ‘The BINGO project-I. Baryon acoustic oscillations from integrated neutral gas observations’. In: *Astronomy & Astrophysics* 664, A14.
- Abdalla, Elcio et al. (2023). ‘BINGO-ABDUS: a radiotelescope to unveil the dark sector of the Universe’. In: *arXiv preprint arXiv:2309.05099*.
- Abdalla, Elcio et al. (2024). ‘BINGO-ABDUS: A Radiotelescope to Unveil the Dark Sector of the Universe’. In: *Compact Objects in the Universe*. Ed. by Eleftherios Papantonopoulos and Nikolaos Mavromatos. Cham: Springer Nature Switzerland, pp. 311–326. ISBN: 978-3-031-55098-0. DOI: 10.1007/978-3-031-55098-0_11. URL: https://doi.org/10.1007/978-3-031-55098-0_11.
- Abdalla, Filipe B. et al. (n.d.). ‘The BINGO project: current status and a proposed extension (ABDUS)’. In preparation.
- Abdalla, Filipe B et al. (2022b). ‘The BINGO Project-III. Optical design and optimization of the focal plane’. In: *Astronomy & Astrophysics* 664, A16.
- (2022c). ‘The BINGO Project-III. Optical design and optimization of the focal plane’. In: *Astronomy & Astrophysics* 664, A16.
- Aghanim, Nabil et al. (2020a). ‘Planck 2018 results-V. CMB power spectra and likelihoods’. In: *Astronomy & Astrophysics* 641, A5.
- Aghanim, Nabil et al. (2020b). ‘Planck 2018 results-VI. Cosmological parameters’. In: *Astronomy & Astrophysics* 641, A6.
- Alam, Shadab et al. (2017). ‘The clustering of galaxies in the completed SDSS-III Baryon Oscillation Spectroscopic Survey: cosmological analysis of the DR12 galaxy sample’. In: *Monthly Notices of the Royal Astronomical Society* 470.3, pp. 2617–2652.
- Anderson, Lauren et al. (2012). ‘The clustering of galaxies in the SDSS-III Baryon Oscillation Spectroscopic Survey: baryon acoustic oscillations in the Data Release 9 spectroscopic galaxy sample’. In: *Monthly Notices of the Royal Astronomical Society* 427.4, pp. 3435–3467.

- Balanis, Constantine A (2016). *Antenna theory: analysis and design*. John wiley & sons.
- Bandura, Kevin et al. (2014). ‘Canadian hydrogen intensity mapping experiment (CHIME) pathfinder’. In: *Ground-based and Airborne Telescopes V*. Vol. 9145. International Society for Optics and Photonics, p. 914522.
- Battye, RA et al. (2013). ‘H i intensity mapping: a single dish approach’. In: *Monthly Notices of the Royal Astronomical Society* 434.2, pp. 1239–1256.
- Benesty, Jacob, Jingdong Chen and Yiteng Huang (2008). ‘Conventional beamforming techniques’. In: *Microphone array signal processing*, pp. 39–65.
- Blake, Chris et al. (2007). ‘Cosmological baryonic and matter densities from 600 000 SDSS luminous red galaxies with photometric redshifts’. In: *Monthly Notices of the Royal Astronomical Society* 374.4, pp. 1527–1548.
- Blas, Diego, Julien Lesgourgues and Thomas Tram (2011). ‘The cosmic linear anisotropy solving system (CLASS). Part II: approximation schemes’. In: *Journal of Cosmology and Astroparticle Physics* 2011.07, p. 034.
- Bogale, Tadilo Endeshaw et al. (2016). ‘On the number of RF chains and phase shifters, and scheduling design with hybrid analog–digital beamforming’. In: *IEEE Transactions on Wireless Communications* 15.5, pp. 3311–3326.
- Bosse, Stéphane et al. (2010). ‘Beamformer ASIC in UHF-L band for the square kilometer array international project’. In: *The 5th European Microwave Integrated Circuits Conference*. IEEE, pp. 106–109.
- Challinor, Anthony and Antony Lewis (2011). ‘Linear power spectrum of observed source number counts’. In: *Physical Review D* 84.4, p. 043516.
- Chen, Xuelei (2012). ‘The Tianlai project: a 21cm cosmology experiment’. In: *International Journal of Modern Physics: Conference Series*. Vol. 12. World Scientific, pp. 256–263.
- Chu, Ta-Shun and Hossein Hashemi (2013). ‘True-time-delay-based multi-beam arrays’. In: *IEEE transactions on microwave theory and techniques* 61.8, pp. 3072–3082.
- Contarini, S et al. (2022). ‘Euclid: Cosmological forecasts from the void size function’. In: *Astronomy & Astrophysics* 667, A162.
- Dawson, Kyle S et al. (2012). ‘The Baryon oscillation spectroscopic survey of SDSS-III’. In: *The Astronomical Journal* 145.1, p. 10.
- Delabrouille, Jacques et al. (2013). ‘The pre-launch Planck Sky Model: a model of sky emission at submillimetre to centimetre wavelengths’. In: *A&A* 553, A96.
- Deshpande, Nitish Vikas, Robert W Heath and Miguel R Castellanos (2022). ‘Nonuniform true time delay precoding in wideband MISO systems’. In: *2022 56th Asilomar Conference on Signals, Systems, and Computers*. IEEE, pp. 1–5.

- Di Dio, Enea et al. (2013). ‘The CLASSgal code for relativistic cosmological large scale structure’. In: *Journal of Cosmology and Astroparticle Physics* 2013.11, p. 044.
- Diacoumis, James AD and Yvonne YY Wong (2019). ‘On the prior dependence of cosmological constraints on some dark matter interactions’. In: *Journal of Cosmology and Astroparticle Physics* 2019.05, p. 025.
- Duane, Simon et al. (1987). ‘Hybrid monte carlo’. In: *Physics letters B* 195.2, pp. 216–222.
- Dutta, Sourjya et al. (2019). ‘A case for digital beamforming at mmWave’. In: *IEEE Transactions on Wireless Communications* 19.2, pp. 756–770.
- Efstathiou, G (2008). ‘Limitations of Bayesian Evidence applied to cosmology’. In: *Monthly Notices of the Royal Astronomical Society* 388.3, pp. 1314–1320.
- Eisenstein, Daniel J et al. (2005). ‘Detection of the baryon acoustic peak in the large-scale correlation function of SDSS luminous red galaxies’. In: *The Astrophysical Journal* 633.2, p. 560.
- El Mrabet, Otman (2006). ‘High frequency structure simulator (HFSS) tutorial’. In: *IETR, UMR CNRS 6164*, pp. 2005–2006.
- Feroz, F, MP Hobson and M Bridges (2009). ‘MultiNest: an efficient and robust Bayesian inference tool for cosmology and particle physics’. In: *Monthly Notices of the Royal Astronomical Society* 398.4, pp. 1601–1614.
- Feroz, Farhan and Mike P Hobson (2008). ‘Multimodal nested sampling: an efficient and robust alternative to Markov Chain Monte Carlo methods for astronomical data analyses’. In: *Monthly Notices of the Royal Astronomical Society* 384.2, pp. 449–463.
- Feroz, Farhan et al. (2013). ‘Importance nested sampling and the MultiNest algorithm’. In: *arXiv preprint arXiv:1306.2144*.
- Fisher, J Richard and Richard F Bradley (2000). ‘Full-sampling array feeds for radio telescopes’. In: *Radio Telescopes*. Vol. 4015. SPIE, pp. 308–318.
- Fisher, Karl B, Caleb A Scharf and Ofer Lahav (1994). ‘A spherical harmonic approach to redshift distortion and a measurement of from the 1.2-Jy IRAS Redshift Survey’. In: *Monthly Notices of the Royal Astronomical Society* 266.1, pp. 219–226.
- Fornazier, Karin SF et al. (2022). ‘The BINGO project-V. Further steps in component separation and bispectrum analysis’. In: *Astronomy & Astrophysics* 664, A18.
- Frid, Henrik (2020). ‘Analysis and optimization of installed antenna performance’. PhD thesis. Kungliga Tekniska högskolan.
- German, S and D Geman (n.d.). ‘Stochastic relaxation, Gibbs distributions, and the Bayesian restoration’. In: *IEEE Trans. Pat. An. Mach. Intell.* (), pp. 721–741.

- Gibson, Peter J (1979). ‘The vivaldi aerial’. In: *1979 9th European Microwave Conference*. IEEE, pp. 101–105.
- Gorski, Krzysztof M et al. (2005a). ‘HEALPix: A framework for high-resolution discretization and fast analysis of data distributed on the sphere’. In: *ApJ* 622.2, p. 759.
- (2005b). ‘HEALPix: A framework for high-resolution discretization and fast analysis of data distributed on the sphere’. In: *The Astrophysical Journal* 622.2, p. 759.
- Gunst, André W, Michiel P van Haarlem and Rene C Vermeulen (2011). ‘LOFAR: A digital aperture array radio telescope’. In: *2011 XXXth URSI General Assembly and Scientific Symposium*. IEEE, pp. 1–1.
- Haarlem, Michael P van et al. (2013). ‘LOFAR: The low-frequency array’. In: *Astronomy & astrophysics* 556, A2.
- Hall, Alex, Camille Bonvin and Anthony Challinor (2013). ‘Testing general relativity with 21-cm intensity mapping’. In: *Physical Review D* 87.6, p. 064026.
- Han, Shuangfeng et al. (2015). ‘Large-scale antenna systems with hybrid analog and digital beamforming for millimeter wave 5G’. In: *IEEE Communications Magazine* 53.1, pp. 186–194.
- Hastings, W. K. (Apr. 1970). ‘Monte Carlo sampling methods using Markov chains and their applications’. In: *Biometrika* 57.1, pp. 97–109. ISSN: 0006-3444. DOI: 10.1093/biomet/57.1.97. eprint: <https://academic.oup.com/biomet/article-pdf/57/1/97/23940249/57-1-97.pdf>. URL: <https://doi.org/10.1093/biomet/57.1.97>.
- Hivon, Eric et al. (2002). ‘Master of the cosmic microwave background anisotropy power spectrum: a fast method for statistical analysis of large and complex cosmic microwave background data sets’. In: *The Astrophysical Journal* 567.1, p. 2.
- Ioushua, Shahar Stein and Yonina C Eldar (2019). ‘A family of hybrid analog–digital beamforming methods for massive MIMO systems’. In: *IEEE Transactions on Signal Processing* 67.12, pp. 3243–3257.
- Jeffrey, Niall and Filipe B Abdalla (2019). ‘Parameter inference and model comparison using theoretical predictions from noisy simulations’. In: *Monthly Notices of the Royal Astronomical Society* 490.4, pp. 5749–5756.
- Jung, Minjae, Hong-Jib Yoon and Byung-Wook Min (2020). ‘A wideband true-time-delay phase shifter with 100% fractional bandwidth using 28 nm CMOS’. In: *2020 IEEE Radio Frequency Integrated Circuits Symposium (RFIC)*. IEEE, pp. 59–62.
- Kaiser, Nick (1987). ‘Clustering in real space and in redshift space’. In: *Monthly Notices of the Royal Astronomical Society* 227.1, pp. 1–21.

- Kang, Xi et al. (2002). ‘An analytical model for the non-linear redshift-space power spectrum’. In: *Monthly Notices of the Royal Astronomical Society* 336.3, pp. 892–900.
- Kant, Gideon W et al. (2011). ‘EMBRACE: A multi-beam 20,000-element radio astronomical phased array antenna demonstrator’. In: *IEEE transactions on Antennas and Propagation* 59.6, pp. 1990–2003.
- Köhlinger, Fabian et al. (2017). ‘KiDS-450: The tomographic weak lensing power spectrum and constraints on cosmological parameters’. In: *Monthly Notices of the Royal Astronomical Society* 471.4, pp. 4412–4435.
- Krolewski, Alex, Simone Ferraro and Martin White (2021). ‘Cosmological constraints from unWISE and Planck CMB lensing tomography’. In: *Journal of Cosmology and Astroparticle Physics* 2021.12, p. 028.
- Leistedt, Boris et al. (2013). ‘Estimating the large-scale angular power spectrum in the presence of systematics: a case study of Sloan Digital Sky Survey quasars’. In: *Monthly Notices of the Royal Astronomical Society* 435.3, pp. 1857–1873.
- Lewis, L, M Fassett and J Hunt (1974). ‘A broadband stripline array element’. In: *1974 antennas and propagation society international symposium*. Vol. 12. IEEE, pp. 335–337.
- Liccardo, Vincenzo et al. (2022). ‘The BINGO project-IV. Simulations for mission performance assessment and preliminary component separation steps’. In: *Astronomy & Astrophysics* 664, A17.
- Lonsdale, Colin J et al. (2009). ‘The murchison widefield array: Design overview’. In: *Proceedings of the IEEE* 97.8, pp. 1497–1506.
- Loureiro, Arthur et al. (May 2019). ‘Cosmological measurements from angular power spectra analysis of BOSS DR12 tomography’. In: 485.1, pp. 326–355. DOI: 10.1093/mnras/stz191. arXiv: 1809.07204 [astro-ph.CO].
- Loureiro, Arthur et al. (2019a). ‘Cosmological measurements from angular power spectra analysis of BOSS DR12 tomography’. In: *Monthly Notices of the Royal Astronomical Society* 485.1, pp. 326–355.
- Loureiro, Arthur et al. (2019b). ‘Upper bound of neutrino masses from combined cosmological observations and particle physics experiments’. In: *Physical Review Letters* 123.8, p. 081301.
- Mailloux, Robert J (2017). *Phased array antenna handbook*. Artech house.
- Marins, Alessandro et al. (2022). ‘Foreground removal and 21 cm signal estimates: comparing different blind methods for the BINGO Telescope’. In: *arXiv preprint arXiv:2209.11701*.
- Massimi, Michela (2021). ‘Cosmic Bayes. Datasets and priors in the hunt for dark energy’. In: *European Journal for Philosophy of Science* 11.1, p. 29.

- McLeod, Michael, Sreekumar T Balan and Filipe B Abdalla (2017). ‘A joint analysis for cosmology and photometric redshift calibration using cross-correlations’. In: *Monthly Notices of the Royal Astronomical Society* 466.3, pp. 3558–3568.
- Mericia, Eduardo J de et al. (2022). ‘Testing synchrotron models and frequency resolution in BINGO 21 cm simulated maps using GNILC’. In: *arXiv preprint arXiv:2204.08112*.
- Metropolis, Nicholas et al. (1953). ‘Equation of state calculations by fast computing machines’. In: *The journal of chemical physics* 21.6, pp. 1087–1092.
- Mudumbai, Raghuraman et al. (2009). ‘Distributed transmit beamforming: challenges and recent progress’. In: *IEEE Communications Magazine* 47.2, pp. 102–110.
- Nan, Rendong et al. (2011). ‘The five-hundred-meter aperture spherical radio telescope (FAST) project’. In: *International Journal of Modern Physics D* 20.06, pp. 989–1024.
- Novaes, Camila P et al. (2022). ‘The BINGO project-VIII. Recovering the BAO signal in HI intensity mapping simulations’. In: *Astronomy & Astrophysics* 666, A83.
- Olivari, LC, M Remazeilles and C Dickinson (2016). ‘Extracting H i cosmological signal with generalized needlet internal linear combination’. In: *MNRAS* 456.3, pp. 2749–2765.
- Padmanabhan, Hamsa, T Roy Choudhury and Alexandre Refregier (2015). ‘Theoretical and observational constraints on the H i intensity power spectrum’. In: *Monthly Notices of the Royal Astronomical Society* 447.4, pp. 3745–3755.
- Padmanabhan, Nikhil et al. (2007). ‘The clustering of luminous red galaxies in the Sloan Digital Sky Survey imaging data’. In: *Monthly Notices of the Royal Astronomical Society* 378.3, pp. 852–872.
- Rahman, B (2020). ‘Time-delay systems: An overview’. In: *Nonlinear Phenomena in Complex Systems* 23.07.
- Remazeilles, Mathieu, Jacques Delabrouille and Jean-François Cardoso (2011a). ‘Foreground component separation with generalized Internal Linear Combination’. In: *Monthly Notices of the Royal Astronomical Society* 418.1, pp. 467–476.
- (2011b). ‘Foreground component separation with generalized Internal Linear Combination’. In: *MNRAS* 418.1, pp. 467–476.
- Rohlfs, Kristen and Thomas L Wilson (2013). *Tools of radio astronomy*. Springer Science & Business Media.
- Rollins, Richard Peter (2015). ‘Chemical and statistical models of interstellar medium and star-forming regions’. PhD thesis. University of London.
- Ross, Nicholas P et al. (2012). ‘The SDSS-III baryon oscillation spectroscopic survey: quasar target selection for data release nine’. In: *The Astrophysical Journal Supplement Series* 199.1, p. 3.

- Rotman, Ruth, Moshe Tur and Lior Yaron (2016). ‘True time delay in phased arrays’. In: *Proceedings of the IEEE* 104.3, pp. 504–518.
- Ruanaidh, Joseph JK O and William J Fitzgerald (2012). *Numerical Bayesian methods applied to signal processing*. Springer Science & Business Media.
- Ruiter, Mark and Erik van der Wal (2009). ‘EMBRACE, a 10000 element next generation aperture array telescope’. In: *2009 European Microwave Conference (EuMC)*. IEEE, pp. 326–329.
- Ruiter, Mark et al. (2016). ‘Development of a Vivaldi tile for the SKA mid frequency aperture array’. In: *2016 10th European Conference on Antennas and Propagation (EuCAP)*. IEEE, pp. 1–4.
- Santos, Marcelo V dos et al. (2024). ‘The BINGO Project-IX. Search for fast radio bursts—A forecast for the BINGO interferometry system’. In: *Astronomy & Astrophysics* 681, A120.
- Santos, Marcelo V dos et al. (2023). ‘The BINGO Project IX: Search for Fast Radio Bursts—A Forecast for the BINGO Interferometry System’. In: *arXiv preprint arXiv:2308.06805*.
- Santos, Mario G et al. (2015). ‘Cosmology with a SKA HI intensity mapping survey’. In: *arXiv preprint arXiv:1501.03989*.
- Schulten, K and RG Gordon (1976). ‘Recursive evaluation of 3j and 6j coefficients’. In: *Computer Physics Communications* 11.2, pp. 269–278.
- Shin, Joon and Daniel H Schaubert (1999). ‘A parameter study of stripline-fed Vivaldi notch-antenna arrays’. In: *IEEE Transactions on Antennas and Propagation* 47.5, pp. 879–886.
- Singh, Tejinder and Raafat R Mansour (2020). ‘Loss compensated PCM GeTe-based latching wideband 3-bit switched true-time-delay phase shifters for mmWave phased arrays’. In: *IEEE Transactions on Microwave Theory and Techniques* 68.9, pp. 3745–3755.
- Skilling, John (2004). ‘Nested sampling’. In: *AIP Conference Proceedings*. Vol. 735. 1. American Institute of Physics, pp. 395–405.
- (2006). ‘Nested sampling for general Bayesian computation’. In: *Bayesian Analysis* 1.4, pp. 833 –859. DOI: 10.1214/06-BA127. URL: <https://doi.org/10.1214/06-BA127>.
- Smolders, AB and GW Kant (2000). ‘Thousand element array (THEA)’. In: *IEEE Antennas and Propagation Society International Symposium. Transmitting Waves of Progress to the Next Millennium. 2000 Digest. Held in conjunction with: USNC/URSI National Radio Science Meeting (C. Vol. 1. IEEE*, pp. 162–165.
- Sohrabi, Foad and Wei Yu (2017). ‘Hybrid analog and digital beamforming for mmWave OFDM large-scale antenna arrays’. In: *IEEE Journal on Selected Areas in Communications* 35.7, pp. 1432–1443.

- Spoof, Kalle et al. (2020). ‘True-time-delay beamforming receiver with RF re-sampling’. In: *IEEE Transactions on Circuits and Systems I: Regular Papers* 67.12, pp. 4457–4469.
- Takahashi, Ryuichi et al. (2012). ‘Revising the halofit model for the nonlinear matter power spectrum’. In: *The Astrophysical Journal* 761.2, p. 152.
- Thomas, Shaun A, Filipe B Abdalla and Ofer Lahav (2011). ‘The angular power spectra of photometric Sloan Digital Sky Survey luminous red galaxies’. In: *Monthly Notices of the Royal Astronomical Society* 412.3, pp. 1669–1685.
- Van Cappellen, WA et al. (2022). ‘Apertif: Phased array feeds for the westerbork synthesis radio telescope-system overview and performance characteristics’. In: *Astronomy & Astrophysics* 658, A146.
- Walker, RC (1999). ‘Very long baseline interferometry’. In: *Synthesis Imaging in Radio Astronomy II*. Vol. 180, p. 433.
- Walters, Anthony et al. (2018). ‘Future cosmological constraints from fast radio bursts’. In: *The Astrophysical Journal* 856.1, p. 65.
- Wu, Fengquan et al. (2021). ‘The Tianlai dish pathfinder array: design, operation, and performance of a prototype transit radio interferometer’. In: *Monthly Notices of the Royal Astronomical Society* 506.3, pp. 3455–3482.
- Wuensche, Carlos A et al. (2022). ‘The BINGO project-II. Instrument description’. In: *Astronomy & Astrophysics* 664, A15.
- Xavier, Henrique S, Filipe B Abdalla and Benjamin Joachimi (2016). ‘Improving lognormal models for cosmological fields’. In: *MNRAS* 459.4, pp. 3693–3710.
- York, Donald G et al. (2000). ‘The Sloan digital sky survey: Technical summary’. In: *The Astronomical Journal* 120.3, p. 1579.
- Zhang, Jiajun et al. (2022). ‘The BINGO project-VI. H I halo occupation distribution and mock building’. In: *Astronomy & Astrophysics* 664, A19.
- Zhang, Xue et al. (2024). ‘The BINGO/ABDUS Project: Forecast for cosmological parameter from a mock Fast Radio Bursts survey’. In: *arXiv preprint arXiv:2411.17516*.
- Zhang, Yongwei et al. (2018). ‘On the front-end design of mid-frequency aperture array for square kilometre array’. In: *Experimental Astronomy* 46, pp. 357–380.
- Zhao, Ze-Wei et al. (2020). ‘Cosmological parameter estimation for dynamical dark energy models with future fast radio burst observations’. In: *The Astrophysical Journal* 903.2, p. 83.